Research Square

Preprints are preliminary reports that have not undergone peer review.
They should not be considered conclusive, used to inform clinical practice,
or referenced by the media as validated information.

FAK- and TGF-β1-dependent biomechanical alterations in microvascular endothelial cells exposed to spatial fluid shear stress gradients

Julio César Sánchez-Rendón
University of Tübingen

Erva Keskin
University of Tübingen https://orcid.org/0009-0000-0787-8340

Nadine Oder
University of Tübingen https://orcid.org/0009-0001-9872-4749

Annalena Reuss
University of Tübingen

Eleftheria Michalaki
Stanford University

Gerald G. Fuller
Stanford University https://orcid.org/0000-0002-2924-053X

Alexander Dunn
Stanford University https://orcid.org/0000-0001-6096-4600

Effie E. Bastounis
effie.bastounis@hu-berlin.de

Humboldt-Universität zu Berlin https://orcid.org/0000-0003-3656-7888

Article

Keywords: Endothelial cells, fluid shear stresses, spatial shear stress gradient, impinging flow, traction force microscopy traction stresses, monolayer stresses, cell biomechanics, rheotaxis, RNA sequencing, FAK, ROCK, TGF-β1, actomyosin contractility

Posted Date: June 26th, 2026

DOI: https://doi.org/10.21203/rs.3.rs-9507974/v1

License: This work is licensed under a Creative Commons Attribution 4.0 International License.
Read Full License

Additional Declarations: There is **NO** Competing Interest.

FAK- and TGF-β1-dependent biomechanical alterations in microvascular endothelial cells exposed to spatial fluid shear stress gradients

Julio César Sánchez-Rendón[1,2], Erva Keskin[1,2], Nadine Oder[1,2], Annalena Reuss[1], Eleftheria Michalaki[3], Gerald G. Fuller[3], Alexander Dunn[3], Effie E. Bastounis[1,2,*]

[1] *Interfaculty Institute of Microbiology and Infection Medicine, Cluster of Excellence "Controlling Microbes to Fight Infections" (CMFI, EXC 2124), Universität Tübingen, 72074, Germany*

[2] *Institute for Biology, Humboldt-Universität zu Berlin, 10115, Germany*

[3] *Department of Chemical Engineering, Stanford University School of Engineering, 94305, USA*

[*] Corresponding Author and Lead Contact:

Effie Bastounis, Ph.D.
Associate Professor in Microbial Infection Biology
Humboldt-Universität zu Berlin
Institut für Biologie
Philippstr. 13 Haus 22
10115 Berlin Germany

Email: effie.bastounis@hu-berlin.de; effie.bastounis@uni-tuebingen.de
Phone: +49 152-26369751

ABSTRACT

Endothelial cells (EC) form a dynamic monolayer barrier that regulates vascular permeability and is highly sensitive to mechanical cues, including shear stress (SS) generated by blood flow. While spatial shear stress gradients (SSG) are strongly linked to vascular pathologies such as atherosclerosis, their direct effects on EC kinematics, mechanics, and signaling, and whether these responses vary across EC subtypes, remain poorly understood. Here, using an impinging flow device compatible with long-term videomicroscopy, we demonstrate that exposure of two distinct EC types to SSG leads to an immediate and sustained two-fold decrease in migration speed, accompanied by enhanced coordination of collective motion and directional migration against the flow. Concurrently, EC traction forces and monolayer stresses increase acutely upon flow onset and continue to rise linearly over time. Mechanistically, FAK-mediated mechanotransduction governs flow-opposed migration, whereas the time-dependent increase in traction depends on TGF-β1 signaling and actomyosin contractility but is not required for setting migration direction. Together, these findings identify SSG as key regulators of EC mechanics, collective dynamics, and signaling, with important implications for vascular disease diagnostics and therapeutic strategies.

KEYWORDS

Endothelial cells, fluid shear stresses, spatial shear stress gradient, impinging flow, traction force microscopy traction stresses, monolayer stresses, cell biomechanics, rheotaxis, RNA sequencing, FAK, ROCK, TGF-β1, actomyosin contractility

INTRODUCTION

Endothelial cells (EC) form a single monolayer lining the inner lumen of blood vessels and serve as a selective barrier that regulates molecular transport while limiting the spread of pathogens and other insults. To fulfill these functions, EC continuously sense and respond to mechanical cues from blood flow, including shear stresses (SS), which regulate major endothelial functions including angiogenesis, vessel remodeling, and even disease progression.ostrowski[1,2-5] Unlike macrovascular EC, which experience relatively uniform flow with nearly constant magnitude SS, microvascular endothelial cells (μEC) in capillary networks are exposed to highly heterogeneous flow environments characterized by steep spatial shear stress gradients (SSG). These gradients naturally arise from vessel bifurcations or curvature, but can also be caused by pathological conditions such as atherosclerosis.[6-8] Despite their (patho)physiological relevance, most studies on endothelial mechanobiology have focused on macrovascular EC exposed to uniform SS, leaving μEC responses to SSG comparatively underexplored.[4,9-11]

To address this gap, an impinging flow device compatible with long-term live-cell microscopy was developed and mounted on multi-well glass-bottom plates, enabling the simultaneous monitoring of multiple conditions.[10,12] This platform was used to study the kinematic response of EC to SSG and was found that lymphatic μEC exhibit density-dependent rheotactic behavior, that is, at high confluency, they migrate against the flow (reverse rheotaxis) and accumulate in regions of high SS, whereas at lower density, they migrate with the flow (forward rheotaxis).[12] Additionally, lymphatic μEC align parallel to flow at low SS but reorient perpendicularly above a critical threshold.[12] Reverse rheotaxis in response to SSG is specific to lymphatic μEC, as macrovascular EC and other cell types migrate with the flow.[10] Constant SS can also stimulate rheotaxis of varying direction depending on the EC origin, with arterial EC exhibiting forward rheotaxis, venal EC reverse rheotaxis and μEC a more complex migratory behavior possibly due to arising gradients.[13]

EC detect SS through a range of surface receptors and mechanosensitive complexes.[14-16] Studies in μEC identified the S1P-S1PR1 axis and shear-correlated calcium signaling as molecular regulators of their response to flow-induced SSG.[11] While additional signaling components may also be implicated, it is unknown how cell-generated forces through alterations in cytoskeletal and focal adhesion dynamics contribute to rheotaxis, and whether similar force-dependent mechanisms operate in other μEC subtypes.[17,18] Given the functional importance of μEC in processes such as wound healing, angiogenesis, and barrier function, deciphering the mechanosensitive migration patterns that operate in response to flow is crucial.

Some insights have come from studies on human umbilical vein EC (HUVEC). Confluent HUVEC increase the traction forces they exert on their matrices and their alignment during prolonged (~24 h) exposure to laminar but not oscillatory shear,[19] as do human pulmonary artery EC.[20] Consistently, another study showed that exposure to constant SS increases HUVEC traction stresses relative to static conditions, with focal adhesion-mediated mechanotransduction being critical in driving cytoskeletal reorganization and polarization along the flow direction.[21] Contrary to these prior studies, another study reported that in HUVEC under laminar flow, both traction and monolayer stresses (inter- and intra-cellular stresses) promptly reduce in magnitude but align along the flow direction, which is followed by HUVEC elongation and alignment.[22] The discrepancies between these studies may likely arise due to experimental differences in SS magnitude, time windows of observation, stiffness of the cells' matrix or confluence. While providing mechanistic insight into biomechanical responses to uniform flow-induced SS, these studies are largely restricted to HUVEC and do not address EC responses to SSG.

In this study, we leveraged an impinging flow device to investigate how SSG influence μEC biomechanics. Collectively, our findings suggest that SSG critically regulate EC rheotaxis, with μEC migrating against the flow direction in a FAK-dependent manner by increasing their traction forces in response to TGF-β1. These insights provide a mechanistic framework for understanding how EC adapt to complex hemodynamic environments, with crucial implications in advancing our understanding of vascular homeostasis and disease progression.

RESULTS

Exposure of μEC to SSG reduces migration speed while enhancing collective motion

To investigate how flow-driven SSG regulate μEC migration, we used human dermal μEC (HMEC-1) and validated key findings also in human cerebral μEC (hCMEC/D3). These two μEC lines were chosen because they have been widely used for studying wound healing, angiogenesis, and barrier function, and because μEC have been shown to experience varying SS and SSG, unlike macrovascular EC whose shear stresses are more uniform.[23] μEC were cultured in monolayer, and an impinging flow device was used to apply flow while enabling concurrent videomicroscopy.[10] Since μEC experience SS between 1-10 dynes/cm², with hypertensive conditions exceeding 30 dynes/cm², we used flow rates mimicking (patho)physiological levels, setting the flow at 3 mL/min.[24-26] This produced the characteristic flow pattern shown in Fig. 1A, with the corresponding SS and SSG profiles shown in Fig. 1B-C.

Exposure to flow resulted in an approximately two-fold reduction in μEC migration speed, which remained remarkably stable throughout the 20 h recording period. This reduction in migration speed was accompanied by a pronounced increase in coordination of cell motion, as evidenced by enhanced alignment of neighboring displacement vectors (Fig. 1D-E, Supplementary Fig. 1A and Supplementarymentary Video 1). In contrast, under static (control) conditions, HMEC-1 and hCMEC/D3 displayed random migration with a progressive decrease in migration speed over time, due to increased cell packing likely resulting from cell proliferation (Fig. 1D-E and Supplementarymentary Fig. 1A). To confirm this hypothesis, we first assessed cell density via flow cytometry at the end of the 20 h recordings. HMEC-1 under flow showed 23% lower density compared to static controls (Supplementarymentary Fig. 1B). We also immunostained HMEC-1 samples for the proliferation marker Ki-67 at 10 h post flow exposure and observed reduced staining in flow-exposed cells compared to static controls (Supplementary Fig. 1C-D).

Considering that flow-exposed μEC appeared to enhance their coordinated motion, we sought to better quantify this observation by calculating the correlation length of neighboring cell displacements vectors (Fig. 1F).[27] We found that throughout the course of the recording, both μEC types exposed to flow exhibited a two-fold increase in their correlation length compared to μEC under static condition. Collectively, these findings demonstrate that flow exposure using the impinging flow device increases μEC migration coordination while reducing and stabilizing migration speed throughout the 20 h of videomicroscopy.

µEC in monolayer reverse rheotax in response to flow-driven SSG

Previous work using an impinging flow device showed that macrovascular EC typically migrate with the flow (forward rheotaxis), while lymphatic µEC migrate against it (reverse rheotaxis).[10] We observed that displacement vectors of both HMEC-1 and hCMEC/D3 pointed toward the jet center under flow, suggesting they undergo reverse rheotaxis, and sought to systematically investigate this behavior in spatiotemporal manner. Exploiting the axisymmetric nature of the impinging flow, we quantified mean radial cell displacements (u_r) as a function of distance from the jet center (or center of the field of view for static controls) and time. These data are represented as kymographs, with time on the horizontal axis and radial position on the vertical axis (Fig. 2A). This approach enables direct visualization and quantification of rheotaxis, where negative u_r (blue) denotes migration toward the jet center, i.e., against the flow.

Under static conditions, both HMEC-1 and hCMEC/D3 showed random migration with no net directional bias, as expected (Fig. 2B-C). In contrast, during flow exposure, both µEC lines consistently exhibited reverse rheotaxis (blue), with HMEC-1 responding faster and showing stronger rheotaxis than hCMEC/D3 (Fig. 2B-C). HMEC-1 rheotaxis peaked in the region between 370 to 555 µm from the jet center, aligning with the region of minimal gradient (Supplementary Fig. 2A). Consistently, imaging fixed HMEC-1 monolayers from the jet center toward the well edge after 20 h of flow revealed a ~20% increase in nuclear density within the high-SSG region compared to static controls, whereas cell densities were comparable between conditions at larger radial distances (Supplementary Fig. 2B-C).

To confirm that reverse rheotaxis results from the SSG and not merely from constant SS due to flow, we exposed HMEC-1 to constant SS (10 and 40 dynes/cm²) using parallel flow channels. Under these conditions, cells showed no changes in migration direction or speed (Supplementary Fig. 2D-E). These results demonstrate that spatial SSG, rather than SS of uniform constant magnitude, are required to induce reverse rheotaxis in µEC within the time frame examined (<40 h).

µEC migration speed partially recovers after flow cessation, while rheotactic directionality persists

To more unambiguously confirm the reduction in µEC migration speed upon flow exposure and to characterize µEC kinematics after flow cessation, we imaged HMEC-1 for 5 h under static

conditions, followed by 20 h of flow exposure (3 mL/min), and then for at least 10 h after flow was ceased (Fig. 3A). This experimental design allowed us to track identical cells within the same field of view before, during, and after flow, excluding confounding effects from variations in cell density or generational differences. Consistent with our earlier observations, HMEC-1 migration speed decreased rapidly and steadily upon flow onset and cells migrated against the flow direction (Fig. 3B-C). Following flow cessation, migration speed partially recovered over time; however, cells continued to migrate directionally against the former flow direction, indicative of persistent reverse rheotaxis, as observed at 35 h, i.e., 10 h after flow cessation (Fig. 3B-C). Furthermore, consistent with this persistent rheotaxis, the correlation length (measure of coordinated motion among neighboring cells) increased during flow exposure and remained significantly higher than in control HMEC-1 never exposed to flow post-flow cessation (Fig. 3D). A similar behavior was observed in hCMEC/D3 (Supplementary Fig. 3A-D, Supplementary Video 2). Together, these results demonstrate that SSG acutely suppress μEC migration speed but induce a persistent rheotactic and collective migration state that outlasts flow exposure, suggesting that μEC retain a mechanical memory of prior flow exposure.

μEC increase traction and monolayer stresses steadily in response to flow-driven SSG

To power their motility, adherent cells exert traction stresses on their extracellular matrix (ECM), which can be thought of as a proxy of how well their focal adhesions are organized and connected to the underlying contractile cytoskeleton.[28] To assess whether changes in traction stresses arise in flow-exposed EC, we applied TFM on a monolayer of HMEC-1 seeded on a soft, physiologically relevant 3 kPa hydrogel embedded with fluorescent beads and performed videomicroscopy both before and after 20 h of flow exposure. We discovered that upon flow exposure, HMEC-1 in a monolayer immediately increased their traction stresses and strain energy (mechanical work imparted by cells to deform their matrix) by ~ 20% (Fig. 4A-C and Supplementary Video 3). This was followed by a continuous time-dependent linear increase in traction stresses and strain energy throughout the exposure to flow, with strain energy reaching ~80% higher values at the end of a 20-hour-long recording. Interestingly, after cessation of flow, HMEC-1 continued to exert elevated traction stresses (for at least the following 10 h that the recordings lasted), which suggest that either the cells have been mechanically reprogrammed and/or their matrix remodeled. A similar mechanical response was observed in hCMEC/D3, although post-flow strain energy returned to near pre-flow values (Supplementary Fig. 4A-B). In contrast, static control EC monolayers exhibited traction stresses and strain energy with minimal temporal fluctuations

(steady) throughout the recordings (Fig. 4A-C, Supplementary Fig. 4B and Supplementary Video 3).

We also performed monolayer stress microscopy (MSM), to calculate EC monolayer stresses (i.e., inter- and intra-cellular stresses), a measure of endothelial barrier integrity strength.[29] Monolayer tensile stresses also increased during flow exposure and remained significantly elevated after flow cessation (Fig. 4A and Supplementary Fig. 4C). Collectively, these data suggest that there is an intricate link between EC kinematics and dynamics during flow exposure. μEC respond immediately to fluid flow-generated shear stress gradients by increasing their traction and monolayer stresses and decreasing their speed as they collectively attempt to reverse rheotax. In other words, it appears that for reverse rheotaxis to occur, cells need to “grab” strongly onto their ECM and move against the flow. Importantly, flow cessation does not fully restore pre-flow mechanical states, indicating persistent biomechanical reprogramming.

SSG upregulate the expression of focal adhesion, cytoskeletal, and --β1-related genes in μEC

The flow-induced increase in traction stresses suggests cytoskeletal reorganization involving focal adhesions and actomyosin contractility. Consistent with this, immunostaining revealed enhanced F-actin stress fibers, increased phosphorylated myosin light chain (pMLC) localization along stress fibers, and a redistribution of vinculin toward basal focal adhesions in flow-exposed μECs, compared with predominantly pericellular vinculin under static conditions (Fig. 5A and Supplementary Fig. 5A-B). To identify mechanotransduction pathways underlying these structural and mechanical changes, we performed RNA sequencing on HMEC-1 and hCMEC/D3 monolayers cultured under static conditions or exposed to flow for 20 h (six biological replicates per condition). Flow exposure induced substantial transcriptional remodeling in both cell types: HMEC-1 exhibited 156 upregulated and 146 downregulated genes, whereas hCMEC/D3 displayed 195 upregulated and 239 downregulated genes, indicating that hCMEC/D3 exhibit greater transcriptional sensitivity to flow compared with HMEC-1 (Fig. 5B-C).

Principal component analysis revealed that the EC type was the primary determinant of transcriptomic variation, accounting for 52% of the total variance, while flow exposure was the second most influential factor, accounting for 13% of variance (Fig. 5D). Given the significant impact of flow on gene expression, we next sought to identify the major biological pathways altered by shear stress. Kyoto Encyclopedia of Genes and Genomes (KEGG) pathway analysis

revealed multiple pathways commonly regulated by flow in both cell types (Fig. 5E and Supplementary Table 1). Among these were pathways directly related to endothelial biomechanics and cytoskeletal regulation, including focal adhesion signaling, cytoskeletal regulation pathways (PI3K-AKT and Hippo), and TGF-β1 signaling (Fig. 5E). Several metabolic pathways (AGE-RAGE, mTOR, FOXO), which can indirectly influence mechanotransduction, were also differentially regulated. In contrast, pathways associated with the mediation of inflammatory responses, such as NF-κB, were suppressed during flow, reinforcing the notion that physiological flow exposure may actually be anti-inflammatory. Among the 142 commonly differentially regulated genes in response to flow, 11 encode proteins involved in ECM remodeling and 23 are associated with TGF-β1 signaling (Supplementary Fig. 5C-D). TGF-β1 is a key cytokine in ECM dynamics that is secreted in a latent form and activated by integrin-mediated cell forces.[30] Several mechanobiologically relevant DEGs support activation of this pathway, including THBS1, which mediates shear-dependent TGF-β1 activation[31,32], JUNB, a regulator of actomyosin contractility [33,34], PDGFB, a mechanosensitive growth factor induced by shear stress[35-37], SMAD7 a regulator of TGFβ signaling[38], IL11, a pleiotropic cytokine secreted in response to TGFβ signaling,[39] and PTGS2, an enzyme rich in breast tumors that expresses high levels of TGF-β1[40]. Conversely, CAV1 (Caveolin-1), which is involved in caveolae formation and mechanosensing, was downregulated, consistent with its suppression by TGF-β1 signaling[41]. Rac2, a small GTPase linked to actin cytoskeleton remodeling, was also downregulated.[42]

Collectively, the transcriptomic analysis suggests that focal adhesion remodeling, cytoskeletal reorganization, and TGF-β1 signaling may be central drivers of μEC adaptation to flow-induced SSG.

FAK inhibition reverses μEC rheotaxis, while ROCK inhibition only slows migration

Based on the observed flow-induced remodeling of focal adhesions and the actomyosin cytoskeleton, we next examined their role in driving reverse rheotaxis and the gradual increase in EC strain energy and mechanistic coupling (Supplementary Fig. 6A). To perturb focal adhesion signaling, HMEC-1 were treated with the focal adhesion kinase (FAK) inhibitor PF-573228 two hours before initiation of videomicroscopy on cells exposed to intermittent flow. FAK inhibition suppressed neither traction force generation before flow exposure, with mean traction stresses remaining comparable to vehicle control, nor traction force increase upon flow exposure and linear increase thereafter (Fig. 6A-B, Supplementary Fig. 6D-F and Supplementary Video 4). However,

traction adhesion turnover (i.e., the extent to which active focal adhesions bearing force renew) was significantly slower upon FAK inhibition (Supplementary Fig. 6G) and was accompanied by a decrease in cell migration speed (Figure 6C). Notably, PF-573228-treated cells failed to exhibit reverse rheotaxis and instead migrated in the direction of flow (Fig. 6D and Supplementary Fig. 6B). Thus, although FAK activity does not regulate the magnitude of traction forces under either static or flow conditions, it is required for dynamic traction adhesion remodeling and for maintaining upstream-directed migration under flow. Moreover, the observation that FAK-inhibited cells retain strong adhesion under both static and flow conditions suggests that migration along the flow direction is not due to weakened adhesions, but instead reflects active forward rheotaxis (i.e., true polarity reversal).

To isolate the contribution of actomyosin contractility independent of focal adhesion signaling, HMEC-1 were treated with the ROCK inhibitor Y-27632. ROCK inhibition significantly reduced the magnitude of cell-generated traction stresses, consistent with previous studies (Fig. 6C and Supplementary Fig. 6D).[43,44] Upon flow exposure, an immediate increase in traction forces was still observed in ROCK-inhibited cells, suggesting that ROCK-independent contractile mechanisms must regulate it (Supplementary Fig. 6E). However, traction magnitude remained constant over time during flow exposure in ROCK-inhibited unlike vehicle control treated cells (Supplementary Fig. 6F and Supplementary Video 4). ROCK inhibition also reduced mean migration speed by approximately 50%, however, ROCK-inhibited cells retained the ability to migrate against the direction of flow, although at reduced speed (Fig. 6D and Supplementary Fig. 6B, C).

Together, these results demonstrate that focal adhesion signaling and actomyosin contractility play distinct roles in μEC rheotaxis. Actomyosin contractility regulates the speed of reverse rheotaxis only, whereas FAK-dependent focal adhesion dynamics are required for rheotaxis directionality. Importantly, the ability of μEC to migrate upstream does not depend on the absolute magnitude of traction stresses, but rather on the dynamic regulation of focal adhesions.

TGF-β1 drives μEC traction strengthening during flow independent of rheotactic response

Since FAK but not ROCK inhibition, failed to suppress the linear increase in traction stresses in flow-exposed μEC (Supplementary Fig. 6F), we next examined whether TGF-β1 signaling contributes to flow-induced traction strengthening, motivated by prior work showing that recombinant TGF-β1 enhances cellular traction forces in other cell types, whereas decreased

traction of ROCK-inhibited cells could inhibit the activation of the TGF-β1 signaling.[33,34] Consistently, treatment of HMEC-1 monolayers with recombinant TGF-β1 under static conditions induced a progressive increase in traction force magnitude over time (Fig. 7A-B). Quantification revealed a ~300% increase in strain energy after 20 h of exposure (Fig. 7C). At later time points (~48 h), cells became highly elongated and exhibited nematic alignment across the monolayer (Supplementary Video 5), consistent with long-term EC cytoskeletal and matrix remodeling.

We then exposed HMEC-1 to flow in the presence of the TGF-β type I receptor inhibitor SB-525334, to examine how that impacts EC traction force generation during flow exposure and rheotaxis. Inhibition of TGF-β1 signaling does not alter the initial acute increase in traction stresses compared to vehicle control treated cells but abolishes the linear increase in traction stresses during flow (Fig. 7D-F and Supplementary Fig. 7A). This indicates that intact TGF-β1 signaling is required for the progressive traction strengthening but not the acute traction response to flow. In contrast, neither mean migration speed nor backward rheotaxis behavior was significantly altered compared with vehicle control-treated HMEC-1 (Supplementary Fig. 7B-C).

Together, these results demonstrate that TGF-β1 signaling is necessary and sufficient for the progressive increase in μEC traction forces observed under flow, but this increase is dispensable for reverse rheotaxis. Thus, traction force strengthening during flow exposure and rheotaxis are likely regulated by distinct mechanotransduction pathways.

DISCUSSION

We report that two distinct μEC types (dermal- and brain-derived) respond to SSG by acutely slowing down and increasing their motion coordination while exhibiting backward rheotaxis. This response is associated with an immediate, time-dependent linear increase in traction and monolayer stresses. Importantly, these biomechanical adaptations persist for at least 10 h after flow cessation, suggesting that μEC retain a mechanical memory of prior flow exposure past.

The acute increase in traction stresses observed in flow-exposed EC is independent of ROCK-mediated contractility or FAK-dependent adhesion reinforcement, motivating the question of what triggers this increase. One speculation is engagement of mechanosensitive elements such as the PECAM-1/VE-cadherin/VEGFR2 complex[12,45] or mechanosensitive ion channels (e.g., Piezo1),[46,47] both of which can alter intracellular tension via calcium influx or myosin light-chain-independent mechanisms, preceding canonical ROCK/FAK signaling.[48] Future studies could address this using Piezo1 inhibitors (e.g., GsMTx4) or genetic knockdown to determine whether mechanosensitive channel activity is required for the acute traction response. Alternatively, traction forces could increase through conformational changes in integrins or adaptor proteins (e.g., talin unfolding) that enhance force transmission to the matrix at existing adhesion sites, bypassing FAK-dependent signaling.[49] In either case, the acute rise in traction stresses likely reflects an active mechanical stabilization of cell-substrate force transmission, enabling EC to rapidly accommodate the sudden and spatially heterogeneous mechanical loads imposed by SSG before slower cytoskeletal and adhesive remodeling takes place.

Concurrently, μEC exhibit an acute but sustained reduction in migration speed accompanied by increased coordination of collective motion as they undergo reverse rheotaxis in response to flow-driven SSG. Reverse rheotaxis has been reported only for cells exposed to uniform SS and for lymphatic EC subjected to SSG[11,13], raising the question of what dictates whether cells migrate with or against the flow direction. Some studies suggest that spatiotemporal activation of both Rho and Rac1 (through PECAM-1 mechanosensing) is required for alignment of EC in the direction of flow and establishment of polarity.[48] Other studies suggest that front-rear polarization in response to flow in varying contexts depends both on Rac1 and FAK signaling.[50-52] This is consistent with our findings, where pharmacological inhibition of FAK inhibits reverse rheotaxis, with cells exhibiting forward rheotaxis albeit with reduced speed. The mechanism by which FAK signaling encodes flow directionality remains unclear. One possibility is asymmetric focal adhesion turnover, with preferential dynamics on the upstream cell edge. Alternatively, direction may be sensed through other mechanisms (glycocalyx, Piezo1), with FAK acting downstream to

execute directional migration. Interestingly, FAK inhibition does not impact the magnitude of traction stresses of cells under static or flow conditions compared to controls, consistent with FAK inhibition not eliminating the mechanochemical responses associated with force generation, recently reported.[53] However, we find that FAK inhibition significantly reduces the turnover of active traction adhesions.

Our observation that ROCK-inhibited cells remain capable of rheotaxis despite exhibiting a ~10-fold reduction in strain energy compared to controls, together with the absence of a linear increase in traction stresses during prolonged flow exposure, indicates that the magnitude of traction forces per se does not determine whether reverse rheotaxis will occur. Moreover, this decoupling raises a related question: why do traction forces progressively increase during flow exposure, and what mechanisms regulate this response if it is dispensable for directional migration? Our transcriptomic and imaging analyses identify TGF-β1 signaling as a key driver of the flow-induced, time-dependent increase in traction stresses independently of reverse rheotaxis, consistent with previous observations in adult fibroblasts.[54]

Since this linear traction stress increase was suppressed upon ROCK inhibition, it is possible that ROCK-inhibited cells are unable to effectively activate latent TGF-β1, which in turn enhances actomyosin contractility and traction generation, further reinforcing TGF-β1 activation.[55-57] When contractility is suppressed, as under ROCK inhibition, traction levels may fall below the threshold required to sustain this feedback loop. This interpretation is consistent with previous reports showing shear-dependent activation of latent TGF-β1 via integrins, as well as shear-regulated TGF-β1 expression and signaling in vascular EC[55] and mesenchymal progenitor cells.[58]

Strikingly, EC retained elevated but stable levels of collective motion coordination as well as high traction and monolayer stresses up to 10h after cessation of flow. This persistence indicates that flow exposure induces a lasting biomechanical state that outlives the external stimulus, consistent with the emergence of a form of mechanical memory. Two, not mutually exclusive, mechanisms could underlie this behavior. First, EC may undergo sustained intracellular reprogramming as a consequence of prior flow exposure, which could be addressed in the future by transcriptomics screening of EC at later times after flow cessation. Alternatively, flow may remodel the ECM of EC, thereby altering the mechanical context to which cells subsequently respond. This hypothesis is supported by our finding that flows upregulates genes related to ECM production. Mechanical memory effects on cells have been reported in other systems, including cells exposed to defined matrix stiffness histories or cyclic stretch,[59,60] and mechanical preconditioning of EC is known to enhance barrier integrity, a principle leveraged in the development of implantable vascular

grafts.[61] Moreover, transient exposure to low shear stress was recently shown to exert long-lasting effects on EC traction forces and alignment under subsequent high-shear conditions.[62] Together, these observations support the idea that transient extracellular physical cues can durably shape EC future behavior. [62]

Although not explored in depth here, differences between the two μEC types were evident. In particular, hCMEC/D3 were transcriptionally more sensitive to flow than HMEC-1 cells, yet, in contrast to HMEC-1, they rapidly returned their traction stresses to baseline following flow cessation. This divergence suggests vascular bed-specific differences in how μEC integrate and respond to mechanical cues, which may reflect distinct mechanosensitive programs tailored to the physiological demands of each bed. In addition, most videomicroscopy experiments were performed either on glass or on compliant 3 kPa substrates. Since matrix stiffness can modulate endothelial mechanosensitivity to flow and cytoskeletal organization, and FAK activation is typically enhanced on stiffer matrices,[63] future studies may address how substrate stiffness modulates flow-guided directional migration.

Finally, transcriptomic analyses revealed that the absence of flow is associated with the upregulation of pathways linked to inflammation and antiviral responses, including interferon signaling as well as NF-κB, JAK-STAT, and NOD-like receptor signaling pathways. These pathways have been implicated in increased endothelial permeability and barrier dysfunction,[64-66] underscoring the critical role of shear flow in maintaining endothelial homeostasis and the importance of incorporating physiologically relevant flow conditions in vitro.

In summary, our findings position spatial SSG as a critical determinant of μEC behavior, capable of reprogramming both cell mechanics and migration patterns. These insights may help explain the spatial heterogeneity of endothelial phenotypes observed in vascular disease. Future studies could explore whether similar SSG-driven adaptations occur in vivo, such as at vessel bifurcations, high-curvature regions, or stenotic lesions, how pulsatile or oscillatory components modulate these responses, and whether interventions targeting FAK or TGF-β1 pathways can restore physiological flow responses in diseased states.

ACKNOWLEDGEMENTS

We are grateful to Julie A. Theriot for her insight, scientific discussions and sharing her resources when those experiments were first conducted. We thank Matthew Footer for discussions, experimental support and assistance for building two replicates of the impinging flow devices. We are grateful to Marie Muenkel and Eduardo Bras for assistance on performing the experiment with the ibidi flow chamber and running COMSOL respectively. We thank Libera Lo Presti for discussions and for revising the manuscript and rest of the materials. We acknowledge that part of our MSM codes are based on the original code (plane stress problem) written by Siva Srinivas Kolukula. The RNA Seq was performed by Arraystar Inc. The graphical abstract was created with BioRender.com. This work was supported at its infancy by the American Heart Association, Award number: 18CDA34070047 (E.E.B.), the Deutsche Forschungsgemeinschaft (DFG, German Research Foundation) under Germany´s Excellence Strategy – EXC 2124 – 390838134 (E.E.B., E.K., A.R., J.C.S.R., N.O.) and by the DFG grant, Project number 532757564 (E.E.B., N.O.). We also acknowledge DFG INST 37/1273-1 FUGG and the Medical Faculty Tübingen. Finally, we acknowledge support by Open Access Publishing Fund of the University of Tübingen.

AUTHOR CONTRIBUTIONS

Conceptualization, E.E.B.; Methodology, E.E.B., E.K., J.C.S.R., E.M., G.G.F., A.R., A.D., E. M., N.O.; Software, E.E.B; J.C.S.R., A.R.; Investigation, E.E.B., J.C.S.R., E.K., A.R., N.O.; Writing – Original Draft, E.E.B., J.C.S.R.; Writing – Review & Editing, E.E.B., E.K., J.C.S.R., E.M., G.G.F., A.D., N.O.; Resources, E.E.B.; Supervision, E.E.B.

COMPETING INTERESTS

The authors declare no competing interests.

CORRESPONDENCE AND MATERIAL REQUEST

Any additional information required to reanalyze the data reported in this paper is available from the lead contact upon request.

MATERIALS AND METHODS

Cell culture conditions

HMEC-1 (a generous gift from the Welch lab, University of California, Berkeley) were cultured in MCDB 131 medium (Gibco, 10372019) supplemented with 10% FBS (Gibco, 21083027), 10 ng/mL epidermal growth factor (Thermofisher, PHG0311), 1 µg/mL hydrocortisone (Fisher, 11444942), and 2 mM L-glutamine (AppliChem, A3704). hCMEC/D3 (a generous gift from the Morrison lab, University of Stuttgart) were cultured according to the manufacturer's instructions (EndoGRO basal medium and EndoGRO MV supplement kit: Millipore, SCME-BM and SCME004-S) with additional 1 ng/mL fibroblast growth factor (Sigma, GF003).

Live-cell videomicroscopy

For all videomicroscopy experiments, we acquired time-lapse phase contrast images of cells (power 15%, exposure time 100 ms) using an inverted Nikon Eclipse Ti2 epifluorescence microscope equipped with a Prime 95B camera (Teledyne Photometrics), and a 10x Plan Fluor DL objective with NA=0.13. The time interval between subsequent image acquisition was always 10 min. The microscope was controlled by the NIS Elements software (Nikon). Temperature was maintained at 37°C throughout the experiment by surrounding the microscope with a box-type incubator (OKOlab). For the traction force microscopy recordings described below, we additionally acquired images of the 0.5 µm fluorescent tracer beads embedded within the hydrogel on which cells were seeded (FITC filter cube with 470/40 excitation and 525/50 emission filters, power 5%, exposure time 80 ms).

Reagents for pharmacological perturbations

Pharmacological inhibitors used during imaging were: Y-27632 (target: ROCK inhibitor, concentration applied to cells: 10 µM, stock concentration: 30 mM in DMSO, source: Tocris, 1254/10); SB-525334 (target: TGF-Smad inhibitor, concentration applied to cells: 10 µM, stock concentration: 30 mM in DMSO, source: Biotechne Tocris, 3211); PF-573228 (target: FAK inhibitor, concentration applied to cells: 5 µM, stock concentration: 100 mM in DMSO, source: Sigma, PZ0117-5MG). All inhibitors in experiments involving flow exposure were added 2 h prior to initiation of videomicroscopy recordings. Recombinant TGF-β1 was added to the cells at the

final concentration of 10 ng/mL 2 h prior to initiation of videomicroscopy recordings (stock concentration: 100 µg/mL in 4mM HCl containing 0.1% BSA, source: R&D systems, 240-B-002).

Perfusion of impinging flow device

One day prior to the application of perfusion, endothelial cells were seeded onto a 20 mm 6-well plate with a 1.5 glass coverslip bottom (CellVis, P06-20-1.5-N). The coverslips were precoated for 30 min at 37°C with rat tail collagen I (Gibco, A10483-01) diluted 1:100 in PBS (Gibco, 10010023). Excess collagen was aspirated, and wells were washed once with PBS before plating $4x10^5$ cells per well (HMEC-1) or $3x10^5$ cells per well (hCMEC/D3) in 500 µL of the corresponding medium. Cells were allowed to adhere, and subsequently each well was filled with additional 2 mL of medium. Cells were then transferred to CO_2-independent Leibovitz's L-15 medium (Gibco, 21083027) with the corresponding supplements and kept for 2 h at 37°C to equilibrate. To acquire images of cells exposed to flow, the 6-well plate with the impinging flow jets on top (orifice located 1 mm above the glass cover slip) was placed on the insert stage of our epifluorescence microscope (Nikon Ti2 Eclipse) and perfusion was started with a flow rate of 3 mL/min (or static/no flow) and maintained for the duration of 20 h. Each time the impinging flow jet device was used, priming was performed before starting cell perfusion experiments, followed by cleaning of the jet device through subsequent washes with autoclaved water and hydrogen peroxide as previously described.[10-12] The simulation of flow pattern and fluid forces generated by the impinging flow device was performed in COMSOL Multiphysics, with use of the module for geometry and material and module for flow simulation for geometry reconstruction and flow pattern calculation, respectively.[10]

Image processing, analysis of cell kinematics and kymographs of cell displacements

Phase contrast images from videomicroscopy recordings were pre-processed with the Fiji/ImageJ software [67] and analyzed using custom MATLAB (Mathworks) scripts. The codes for this analysis are available in our GitHub repository (see DOI:10.5281/zenodo.7155531). Using MATLAB, background and flatfield corrections were applied using a pseudo-flatfield correction with gaussian filter and a standard deviation of 40 pixels. Cell displacements were then calculated over time using a custom script for particle image velocimetry (PIV) in MATLAB.[68] For PIV on the phase contrast images, we always used a window size of 48 px and an overlap of 24 px. Displacements on the cartesian coordinate system were calculated and plotted on top of the phase contrast images using vector arrows. The superimposed white concentric rings resulting from this type of

analysis indicate the different shear stress zones (185 μm apart) (Fig. 1A-C). We then moved from a cartesian coordinate system to a polar one, to be able to calculate radial displacements and depict mean radial displacements over time using a kymographic representation. Average radial displacements (u_r) of the cells are shown as a function of distance from the jet orifice (which is always located at the center of the field of view imaged) and over time, with negative displacements indicating cell migration towards the jet center, that is, against the flow, and positive displacements indicating migration away from the center, that is, in the direction of the flow. Finally, using an additional custom-built script in Matlab (Mathworks), we calculated coordination length and cell migration speeds. Correlation length was calculated as the spatial correlation function $C_{dd}(R)$ that averages the scalar product of all vector pairs separated by a distance R. The correlation values show an exponential decay over distance that can be fitted to the function $C_{dd}(R) = \exp(-R/R0)$, where $2R0$ indicates the maximum non-random correlated distance [27]. Cell migration speed was calculated as the median value of the distribution generated from the magnitude of the displacement vectors (through PIV) divided by the time between successive frames (10 min). Median values of cell migration speed for each time point and for multiple independent experiments was visualized using Graphpad Prism v10, showing the mean value for different experiments ±SEM. To assess how time and radial position impact the direction of cell migration of flow-exposed cells, the calculated kymographs were further processed. First, we calculated the sum of the mean radial cell displacements across all the radial positions for a given time point and plotted it as a function of time (Fig. 2A). A similar procedure was followed to quantify the impact of shear stress magnitude on cell migration direction (related to the radial position). In particular, all mean radial displacements across all time points were summed up and plotted as a function of radial position (Supplementary Fig. 2A).

Perfusion of ibidi flow device and image analysis

We used a μ-Slide VI 0.4 glass bottom channel slide pre-coated with Collagen I (Ibidi GmbH; cat. # 80606; channel volume 30 μL, height 0.4 mm, width 3.8 mm) to seed cells and subsequently expose them to constant magnitude shear stress. In each channel, we seeded $1x10^5$ cells in 30 μL (HMEC-1). The cells were let to adhere for ~ 30 min, and then additional 60 μL of cell culture medium was added to the inlet and outlet of each of the six channels. Twenty-four hours after cell seeding, cells had formed a monolayer, and the medium was changed to Leibovitz's L-15 medium (Fisher, 11540556) with the corresponding supplements. Subsequently, the ibidi Pump System (Ibidi GmbH, 10902) was assembled and connected to the μ-Slide, which was then placed at the

insert stage of our epifluorescence microscope. Live cell imaging was conducted as described above, using a 10x Plan Fluor DL objective with NA=0.13. In the acquired phase contrast images, flow direction was from the bottom to the top of the field of view. In most recordings, and unless otherwise indicated, cells were first kept under stationary conditions (1-3 h), then exposed to constant magnitude fluid shear stress of 10 dynes/cm^2 for 20 h, and finally to constant magnitude fluid shear stress of 40 dynes/cm^2 for additional 20 h. Kinematical analysis of cell motion was conducted as described above.

Traction force and monolayer stress microcopy (TFM and MSM)

Polyacrylamide hydrogels were prepared as previously described [69]. Glass-bottom plates with 6 wells (Cellvis, P06-1.5H-N) were incubated for 30 min with 500 µL of 0.5 M NaOH, then rinsed with distilled water, and incubated with 500 µL of 2% 3-aminopropyltriethoxysilane (Sigma, A3648) in 95% ethanol for 5 min. Following rinsing with water, 500 µL of 0.5% glutaraldehyde (Sigma-Aldrich, G6257) were added to each well for 30 min. Wells were rinsed with water again and dried at 60°C. To prepare polyacrylamide hydrogels of 3 kPa, two mixtures were prepared containing 5% acrylamide (Sigma, A4058) and 0.1% bis-acrylamide (Fisher, BP1404-250) [69], the second of which additionally contained 0.03% of 0.5 µm fluorescent tracer beads (Invitrogen, F8813) for TFM experiments. To initiate polymerization 0.06% ammonium persulfate (Fisher, BP17925) and 0.43% TEMED (Signs-Aldrich, 110732) were added to the mixtures. First, 3.6 µL of the first mixture without the beads was added at the center of each well, capped with 18-mm untreated circular glass coverslips, and allowed to polymerize for 20 min. After coverslip removal, 3.6 µL of the mixture containing tracer beads was added and sandwiched again with an 18-mm untreated circular glass coverslip and allowed to polymerize for 20 min. Next, 50 mM HEPES (Roth, HN78.3) at pH 8.5 was added to the wells, and coverslips were removed. Hydrogels were UV-sterilized for 1 h and then activated by adding 500 µL of 0.1% weight/volume heterobifunctional cross-linker Sulfo-SANPAH (ProteoChem, c1111) in 1% dimethyl sulfoxide (DMSO) (Sigma, D2650) and 50 mM HEPES, pH 8.5, on the upper surface of the hydrogels, followed by exposure to UV light for 10 min. Hydrogels were washed with 50 mM HEPES at pH 8.5 and coated with 500 µL of 0.25 mg/ml rat tail collagen I in 50 mM HEPES at pH 8.5 overnight at room temperature. The next morning, the collagen I-coated surfaces were washed with HEPES, and gels were stored in 50 mM HEPES solution.

TFM was performed as previously described.[70,71] Briefly, in TFM, cells actively pull on the elastic hydrogel containing fluorescent tracer beads depending on how well their focal adhesions are

organized and connected to the underlying cytoskeleton. The resulting traction stresses can be analytically calculated from the measured displacements of hydrogel-embedded beads.[70,72] Prior to seeding the cells, hydrogels were equilibrated with cell medium for 30 min at 37°C. Cells were then seeded to a specific concentration to yield 100% confluent monolayers 24 h later. Specifically, 24 h prior to live-cell imaging, HMEC-1 and hCMEC/D3 were seeded directly onto the hydrogels at a density of $4x10^5$ cells and $3x10^5$ cells per well, respectively. Cells were exposed to flow 2-5 h after the start of the microscopy recording acquisitions (as indicated in the corresponding figure legends) and were imaged under these conditions for a period of 20 h. Afterwards, flow was ceased, and cells were imaged for additional 10 h to evaluate their recovery. Multi-channel time-lapse sequences of fluorescence (to image the beads within the upper portion of the hydrogels) and phase contrast images (to image the cells) were acquired using an inverted Nikon Eclipse Ti2 with a Prime 95B sCMOS camera and a 10x 0.13NA Plan Fluor air objective. The microscope was controlled by the NIS Elements software. Temperature was maintained at 37°C throughout the experiment. Images were acquired every 10 min for approximately 30 h. Subsequently, at each time interval, we measured the 2D deformation of the substrate using an image correlation technique similar to particle image velocimetry. We calculated the local deformation vector by performing image correlation between each image and an undeformed reference image which we acquired by adding 200 µL of 10% w/v sodium dodecyl sulfate (SDS) (Roth, 2326.2) at the end of each recording to detach the cells from the hydrogels. We used interrogation windows of 32 x 16 pixels (window size x overlap). Calculations of the two-dimensional traction stresses that cell monolayers exert on the hydrogel are described elsewhere.[71,72]

We calculated the strain energy (U_s) as the mechanical work imparted by cells to deform the hydrogel as $U_s = \frac{1}{2} \int \boldsymbol{t}(z = h) \cdot \boldsymbol{u}(z = h) ds$, where $\boldsymbol{u}(z = h)$ is the measured displacement vector fiel on the free surface of the hydrogel, $\boldsymbol{t}$ is the calculated traction stress vector field, $\int_s ds$ represents the surface integral, h is the height of the hydrogel and z the vertical coordinate. For each field of view analyzed originating from different wells we normalized the strain energy value with that of time = 0 min, to avoid discrepancies due to slight differences in cell confluence among wells. To compare the relative increase in strain energy upon flow application of vehicle control treated to cells treated with different pharmacological inhibitors, we averaged the normalized strain energy values one hour prior to flow application and one hour immediately after flow application and calculated their ratio (Supplementary Fig. 6E). To compare the relative increase in strain energy during the 20 h period of flow application of vehicle control treated to cells treated

with different pharmacological inhibitors, we averaged the normalized strain energy values one hour immediately after flow application and one hour before flow cessation and calculated their ratio (Supplementary Fig. 6F).

We used Monolayer Stress Microscopy (MSM) to infer the EC monolayer tensile and compressive stresses from the traction stresses EC exert on the hydrogel as done previously.[73,74] Monolayer stresses (σ) are calculated from the system of equations composed by the Beltrami differential equation and Newton's equilibrium equations. This formulation only requires the traction stresses (τ) in both the x and y directions, the cell's Poisson's coefficient (ν), and the monolayer thickness (h). This model considers the following assumptions: perfect cell-cell adhesions (monolayer is a continuum), perfect cell-substrate adhesions (traction forces are balanced with monolayer stresses), monolayer thickness is uniform and constant (uniform properties), cells are considered linear elastic isotropic material, traction stresses are generated only in the plane of the monolayer and negligible in the vertical direction (the normal component of traction forces is negligible), and time-dependent changes in monolayer configuration and strains are small (small strain assumption). Displacements along the edge of the monolayer/image were set to zero while Poisson's coefficient and monolayer thickness were set to 0.48 and 10 μm, respectively. Finally, we transformed the monolayer stresses from the cartesian coordinate system (x,y) to the principal coordinate system (I, II). This new system does not consider the shear component of stress and allows for the computation of the maximum monolayer tension (σ_I) and compression (σ_{II}). Mathematical derivation of the model is described elsewhere [73]. We used a custom Matlab (MathWorks) script with a finite element implementation of the mentioned model to calculate the monolayer stresses at each time point. The source code is provided at https://github.com/ebastoun/Monolayer-Stress-Microscopy (DOI:10.5281/zenodo.7155523).

Characterization of traction adhesion dynamics

To quantify how dynamic the active focal adhesions of EC are, we performed cross-correlation analysis on subsequent maps of EC traction stress magnitude. We assumed that less dynamic traction forces would result in successive images with high similarity (stable focal adhesions, high correlation) while highly dynamic traction forces would result in images with low similarity (dynamic focal adhesions, low correlation). The cross-correlation coefficient was calculated between a given frame and the next 20 successive frames (lag). Then, we created a kymographic representation of the magnitude of the correlation coefficient as a function of lag (y-direction) and

time (x-direction). The cross-correlation analysis and the kymograph were performed using a custom Matlab (MathWorks) script.

Immunofluorescence microscopy, nuclear segmentation, and quantitative analysis of cytoskeletal organization

HMEC-1 residing on glass substrates were incubated with 1 µg/mL Hoechst to stain the cells' nuclei for 10 min at 37°C prior to fixation. The following steps were carried out at room temperature. Cells were washed with PBS and fixed with 4% EM grade formaldehyde (Thermofisher, 28906) in PBS for 10 min. Following a wash with PBS, samples were permeabilized for 5 min in 0.2% Triton X-100 (Roth, 3051.4) in PBS and washed again with PBS. Samples were then blocked for 30 min with 5% BSA (AppliChem, A6588) in PBS and then incubated for 1 h with primary antibodies (pMLC: Cell signaling technology, 3671, RRID: AB_330248; vinculin: Sigma, V9131-2ML, RRID: AB_477629) diluted 1:100 in PBS containing 2% BSA. For actin staining, we used 0.2 µM AlexaFluor488 phalloidin (Thermo Fisher, A12379). Samples were washed three times in PBS and then incubated for 1 h with secondary antibodies diluted 1:250 in PBS containing 2% BSA. We used goat anti-mouse Alex Fluor 647 (Thermofisher, A32728, RRID: AB_2633277) and goat anti-rabbit Alex Fluor 546 (Thermofisher, A11035, RRID: AB_2534093). Samples were washed three times in PBS and then stored in 2 mL PBS at 4°C until imaging. For epifluorescence imaging, we used an inverted Nikon Eclipse Ti2 with a Prime 95B sCMOS camera, 40x 0.60NA Plan Fluor air or a 20x 0.75NA Plan Apo air objective and NIS Elements software. For automated nuclear cell segmentation, we used the cellC software run in Matlab (Mathworks).[75] For quantification of fluorescence intensity of either vinculin, F-actin or pMLC per cell, a custom built code in Matlab (Mathworks) was used.

RNA isolation and RNA sequencing

Sample Preparation: HMEC-1 and hCMEC/D3 cells were placed at a concentration of $2x10^5$ and $1x10^5$ cells/well on 20 mm collagen I-coated glass coverslips of 6-well plates for 48 h until they form a confluent monolayer. Subsequently they were exposed for 20 h to flow (3 mL/min, using the impinging flow jet device) or not for the static controls. Cells were then harvested and lysed using the QIAshredder Kit (Qiagen; 79656). We analyzed N=6 samples per condition, so had a total of 24 samples. mRNA was harvested using the RNeasy Plus Micro Kit (Qiagen; 74004) and eluted in 30 µL RNase free water. Cells in solution were spun down and lyzed using the QIAshredder Kit (Qiagen; 79656). mRNA was harvested using the RNeasy Plus Micro Kit

(Qiagen; 74004) and eluted in 30 µL RNase free water. A NanoDrop ND-1000 spectrophotometer was used to determine concentration (abs 260) and purity (abs260/abs230) of total RNA samples. Agarose gel electrophoresis was used to check the integrality of total RNA samples (performed by Arraystar Inc.).

RNA library preparation and RNA sequencing: The total RNA was depleted of rRNAs using the Arraystar rRNA Removal Kit. We used Illumina kits for the RNA-seq library preparation, which included RNA fragmentation, random hexamer primed first strand cDNA synthesis, dUTP based second strand cDNA synthesis, end-repairing, A-tailing, adaptor ligation and library PCR amplification. The resulting RNA-seq libraries were qualified using Agilent 2100 Bioanalyzer and quantified using the qPCR absolute quantification method. Sequencing was performed using Illumina NovaSeq 6000 and the High-Output Kit with 2x150 read length. We had an average of 40 million reads per sample. The DNA fragments in well mixed libraries were denatured with 0.1M NaOH to generate single-stranded DNA molecules, loaded onto channels of the flow cell at 8 pM concentration, and amplified in situ using TruSeq SR Cluster Kit v3-cBot-HS (#GD-401-3001, Illumina). Sequencing was carried out by running 150 cycles on the Illumina X-ten/NovaSeq according to the manufacturer's instructions.

Sequencing data analysis: The raw sequencing data that passed the Illumina chastity filter were used for the following analysis. Trimmed reads (trimmed 5', 3'-adaptor bases) were aligned to the reference genome (GRCh37). Based on alignment statistical analysis (mapp.i.ng ratio, rRNA/mtRNA content, fragment sequence bias), we determined whether the results were suitable for subsequent data analysis. To examine the sequencing quality, the quality score plot of each sample was plotted. The quality score Q is logarithmically related to the base calling error probability (P): $Q = -10\log_{10}(P)$. For example, Q30 means the incorrect base calling probability to be 0.001 or 99.9% base calling accuracy. After quality control, the fragments were 5', 3'-adaptor trimmed and filtered ≤ 20 bp reads with Cutadapt software. The trimmed reads were aligned to the reference genome with Hisat 2 software. In a typical experiment, it is possible to align 40 to 90% of the fragments to the reference genome. However, this percentage depends on multiple factors, including sample quality, library quality and sequencing quality. Sequencing reads are classified into the following classes: (1) mapped: reads aligned to the reference genome (including mRNA, pre-mRNA, poly-A tailed lncRNA and pri-miRNA); (2) mtRNA and rRNA: fragments aligned to rRNA, mtRNA; and (3) unmapped: reads that are not aligned.

Differentially expressed genes (DEGs) and differentially expressed transcripts were calculated. Novel genes and transcripts were also predicted. The expression level (FPKM value) of known

genes and transcripts was calculated using ballgown through transcript abundances estimated with StringTie. The number of identified genes and transcripts per group was calculated based on the mean of FPKM in group ≥ 0.5. Fragments per kilobase of transcript per million mapped reads (FPKM) were calculated with the formula: $\boldsymbol{FPMK} = \frac{\boldsymbol{C} \times \mathbf{10^6}}{\boldsymbol{L} \times \boldsymbol{N}}$, where C is the number of fragments that map to a certain gene/ transcript, L is the length of the gene/transcript in Kb and N is the number of fragments that map to all genes/transcripts. Differentially expressed gene and transcript analyses were performed with R package ballgown and both p- and q-values were calculated. Because the DEG listed identified was used for pathway enrichment analysis as discussed below, p-value cutoff was used. Fold change (cutoff 1.5), p-value (≤ 0.05) and FPKM (≥ 0.5 mean in one group) were used for filtering differentially expressed genes and transcripts.

Pathway enrichment and gene ontology (GO) analysis

Kyoto Encyclopedia of Genes and Genomes (KEGG) pathway and Gene Ontology (GO) term analyses of the whole data set of DEG were performed using the R package GAGE "Generally Acceptable Gene set Enrichment" (GAGE v.2.22.0) package implemented in R. Briefly, default parameter settings were used for comparisons of log-scaled gene set expression (i.e. enrichment) data between different flow conditions (q-value <0.01). Gene sets were defined using annotations obtained from GAGE v2.22.0, go.db v3.2.2, and kegg.db v3.2.2. The R package "Pathview" v.1.12.0 and KEGGGraph v1.30.0 were used to visualize gene set expression data in the context of functional pathways.

Determination of shared DEGs and pathways across cell types in response to flow

As a pre-processing step, information on differentially expressed genes, pathways, cell type, fold change and enrichment score obtained from the gene set analysis was organized into a table format in Microsoft Excel. A custom R v4.3.3 script was used to process said tables to find common differentially expressed genes and related pathways. Briefly, an undirected graph (igrap v2.0.3 package) was constructed from an ordered list of cell types and genes (or pathways). Histograms of fold change for commonly differentially expressed genes and pathway enrichment score were plotted with ggplot2 v3.5.1 package.

Assessment of cell proliferation through Ki-67 immunostaining and flow cytometry

To qualitatively assess whether the proliferation rate of HMEC-1 cells changed due to exposure to fluid flow as compared to stationary conditions, we first performed immunostaining for the proliferation marker Ki-67. To that end, cells were fixed directly after flow priming for 10 h or not (static condition) using 4% formaldehyde in PBS for 10 min at room temperature. The cells were then permeabilized with 0.2% Triton X-100 in PBS for 5 min and washed with PBS. Subsequently, samples were blocked with 5% BSA in PBS for 30 min and incubated with the primary anti-Ki-67 rabbit antibody (Invitrogen, MA514520, RRID: AB_10979488) at a 1:100 dilution in 2% BSA in PBS for 1 h. The samples were washed three times with PBS and blocked again with 5% BSA for 30 min. Finally, the cells were incubated with a goat anti-rabbit-488 antibody (1:250) (Thermofisher, A-11008, RRID: AB_143165) and DAPI (1:1000) for 45 min. After washing three times with PBS, the samples were stored in PBS and imaged using an inverted Nikon Eclipse Ti2 epifluorescence microscope with a Prime 95B sCMOS camera, a 40x 0.60NA Plan Fluor air objective, and the NIS Elements software. For quantitative assessment, nuclear regions of interest (ROIs) were generated in Fiji (ImageJ) based on DAPI staining. After background correction, z-stacks were maximum intensity projected, and mean nuclear Ki-67 fluorescence intensity was measured for each segmented nucleus. To define Ki-67 positivity, mean nuclear Ki-67 intensity values from pooled static samples were used to calculate the 80^{th} percentile, resulting in a fixed threshold of ≥1762 arbitrary units (a.u.). This threshold was applied consistently across both conditions. The percentage of Ki-67-positive nuclei per image was calculated as the ratio of nuclei with mean Ki-67 intensity ≥1762 a.u. to the total number of nuclei.

Flow cytometry analysis on whole cell samples primed with flow for 20 h or not (static condition) was also performed in sextuplicate. To that end, HMEC-1 cells were first washed with PBS and then incubated with 0.25% trypsin-EDTA (Thermofisher; 25200056) for 15 min to detach cells from the glass bottom dishes. Trypsin was neutralized with the addition of MCDB medium containing FBS, and cell suspensions were pipetted up and down six times to disperse cell clumps. Cells were strained into 5 mL polystyrene test tubes through a cell strainer snap cap with a 35 µm nylon mesh (Fisher scientific; 352235), and flow cytometry analysis was performed on a BD LSRFortessa X-20 in high acquisition mode with a flow rate of 60 µL/min. To obtain a pure cell population (and not debris), events were gated based on the SSC vs FSC scatter plot, with a total of 10,000 events recorded per sample. The population was plotted using the FSC against time, and the cell count passing through the flow cell within 10 s was determined using the FlowJo software (BD Life Sciences). Cell density was calculated for each sample assuming a flow rate of 60 µL/min. The values were normalized to the mean of the static samples for each experiment.

Statistical analysis

Statistical analyses were performed with Graphpad Prism 10 (RRID: SCR_002798). Differences in data distributions were determined to be statistically significant when $p < 0.05$: *, $p<0.01$: **, $p<0.001$: *** and $p<0.0001$: **** by running a non-parametric Wilcoxon rank sum test (WRST) or, in case of multiple comparisons, a Kruskal-Wallis test with Dunn's multiple comparison test (denoted as KWTD), as indicated. Statistical parameters are reported in the figure legends. Bar plots with error bars show mean and standard deviation (SD) or standard error of the mean (SEM), circles represent mean values of independent microscopy recordings for the corresponding time intervals of each bin (e.g., see Fig. 4c).

Data and code availability

Data collected and computer codes are available on request to the corresponding authors. Codes are also publicly available as described below. (1) Cell kinematics analysis (DOI:10.5281/zenodo.7155531); (2) Construction of kymographs and additional analysis based on those (DOI:10.5281/zenodo.19386424). (3) Monolayer stresses calculation (DOI:10.5281/zenodo.7155523). The RNA sequencing data (FASTq files) generated during this study and subsequent analysis are available at the Gene Expression Omnibus (GEO) database (Accession ID: GSE206571, access token: ahsraiwmltarfkp). All differential expression analysis results of this study are included as a supplementary table in this article. Any additional information required to reanalyze the data reported in this paper is available from the lead contact upon request.

FIGURES AND FIGURE LEGENDS

Figure 1

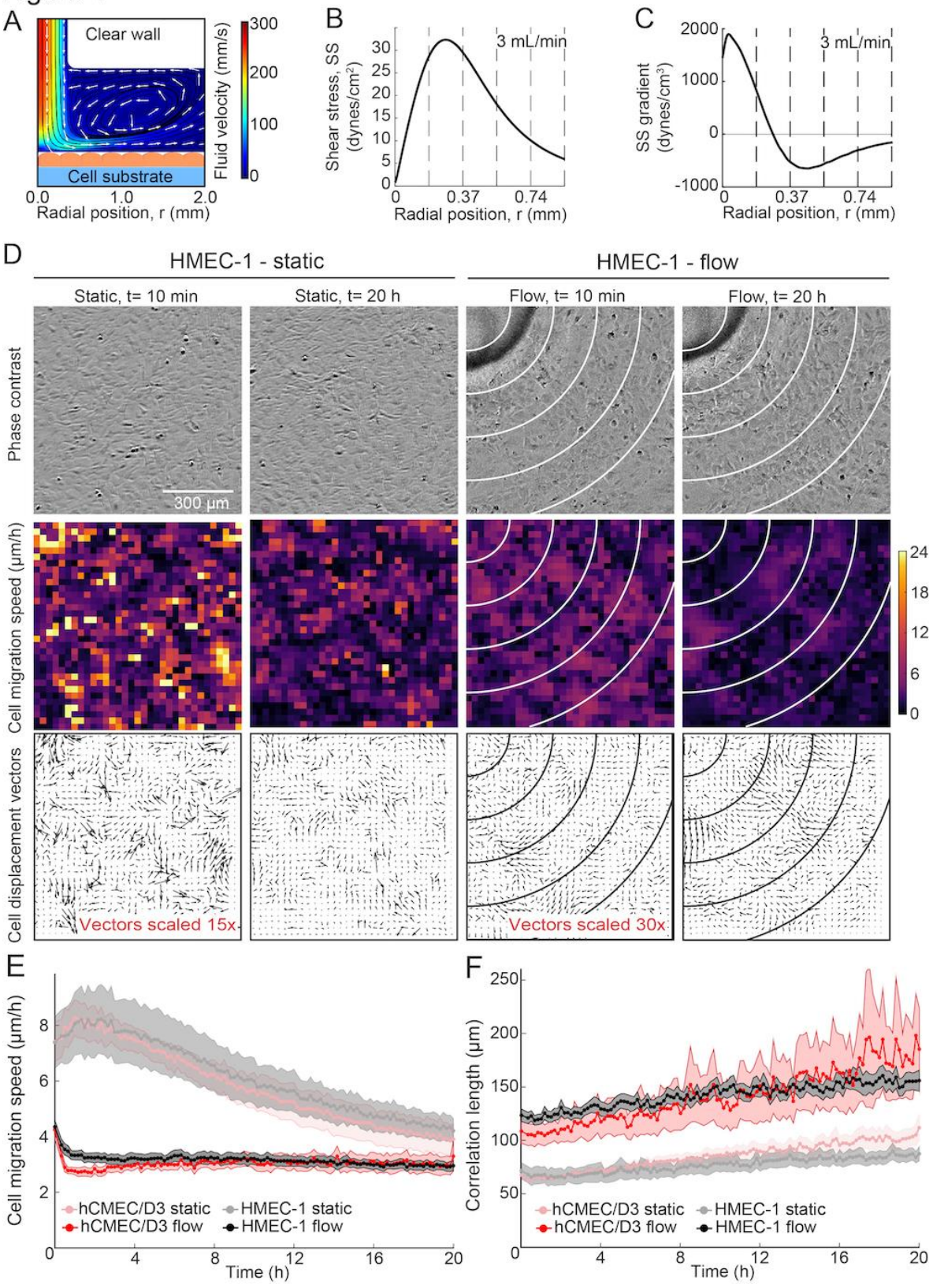


Fig. 1: SSG slows µEC migration speed while enhancing motion coordination.

A Finite element simulation of the cross-sectional flow velocity profile and fluid streamlines (white arrows) at 3 mL/min flow rate, illustrating the spatially varying axisymmetric flow experienced by cells using the impinging flow jet device. **B-C** Simulated SS (B) and SSG (C) as a function of the radial distance from the stagnation point (*r*=0 µm) situated directly below the flow orifice center at a 3 mL/min flow rate. **D** Representative phase contrast images, cell migration speed (µm/h), and cell displacement vectors (calculated from consecutive frames acquired 10 min apart) for HMEC-1 in monolayer at t=10 min and t=20 h under static (columns 1, 2) or flow exposed conditions (columns 3, 4). Jet center positioned at the center of the field of view imaged, but only a quarter of the field of view is shown. White or black contours mark concentric regions spaced 185 µm apart from the jet orifice. Cell displacements are scaled 15x and 30x larger for static and flow-exposed cells, respectively. **E** Cell migration speed (µm/h) over time (h) for HMEC-1 (black) and hCMEC/D3 (red) under static and flow conditions (opaque vs. bright lines). Data represent mean±SEM of n=10±4 recordings from at least N=3 independent experiments. **F** Same as panel E but showing correlation length of cell motion (µm) over time (x-axis, h).

Figure 2

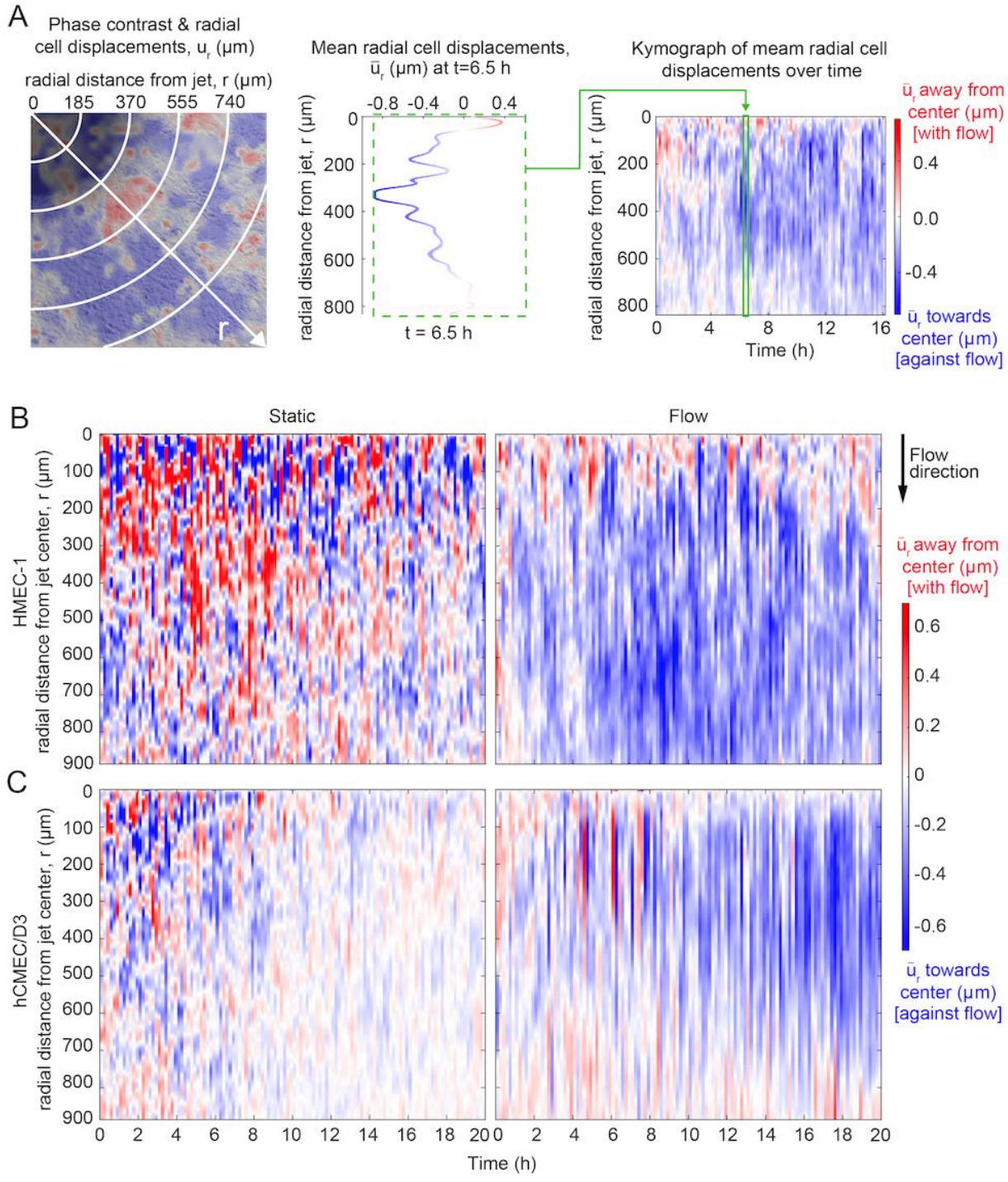


Fig. 2: µEC in monolayer exposed to SSG migrate collectively against the flow direction. **A** Left: phase contrast image of HMEC-1 in monolayer with superimposed radial cell displacement map, u_r (µm), where blue indicates cell movement toward the jet center (negative u_r) and red indicates movement away from the jet center (positive u_r). Middle: Plot of mean u_r, along the radial

direction, as a function of radial distance from the jet center at a specific time point (blue for negative and red for positive mean u_r). Right: Sequential measurements of mean radial cell displacements u_r (µm) stacked next to each other over time (h) enable the construction of a kymograph showing spatiotemporal evolution of radial cell displacements, u_r (y-axis: radial distance r, µm; x-axis: time h). **B** Kymograph of the mean radial cell displacements, u_r (in µm, see colorbar) for HMEC-1 in monolayer under static (left) or flow (right) conditions. The center of the polar coordinate system is at the center of the field of view (where the orifice of the jet is for flow exposed cells). **C** Kymograph as panel B but for hCMEC/D3. Kymographs are representative of n=10±4 recordings from at least N=3 independent experiments.

Figure 3

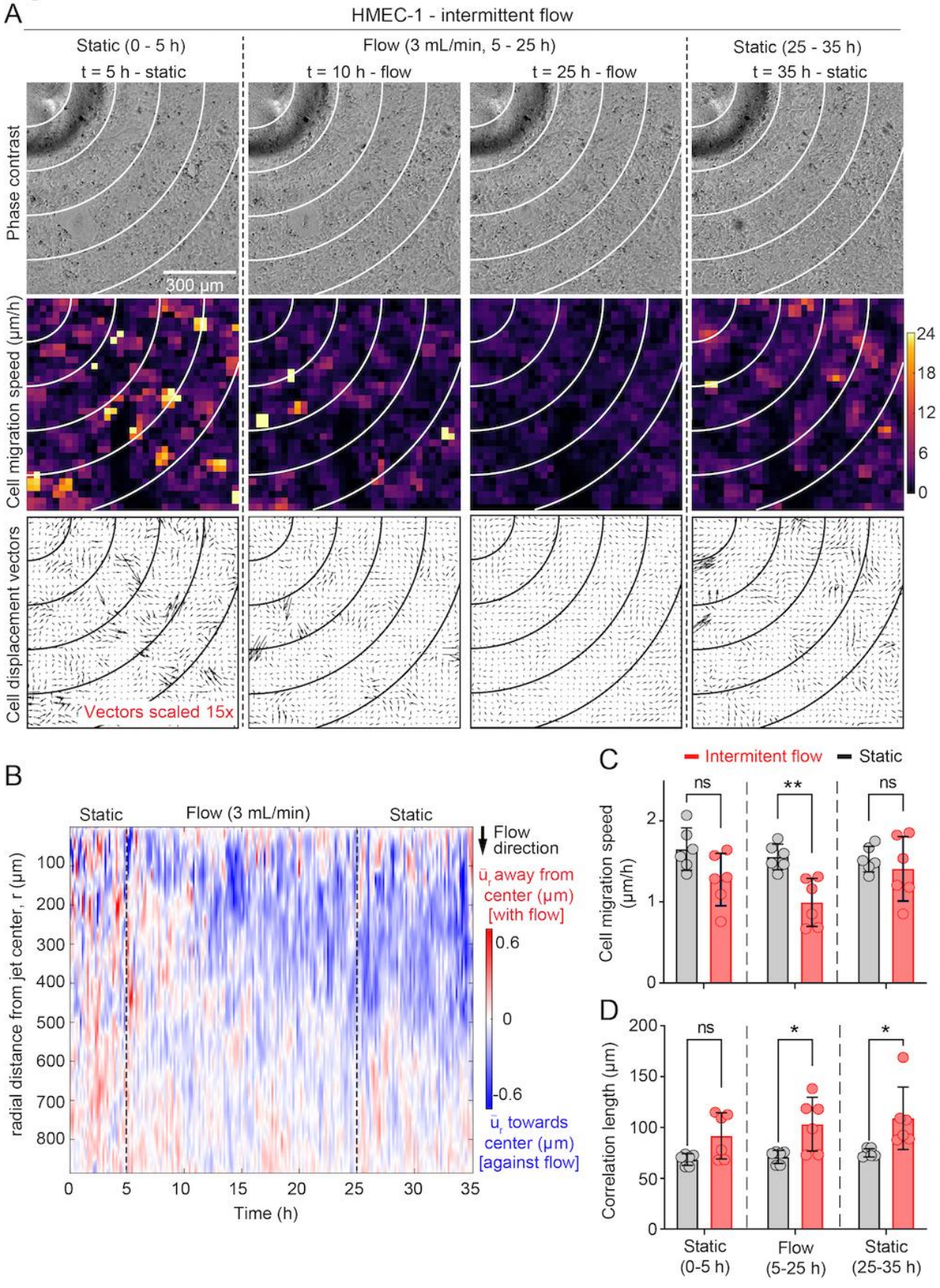

A
HMEC-1 - intermittent flow
Static (0 - 5 h)
Flow (3 mL/min, 5 - 25 h)
Static (25 - 35 h)
t = 5 h - static
t = 10 h - flow
t = 25 h - flow
t = 35 h - static
Phase contrast
300 µm
Cell migration speed (µm/h)
24
18
12
6
0
Cell displacement vectors
Vectors scaled 15x
B
Static
Flow (3 mL/min)
Static
radial distance from jet center, r (µm)
100
200
300
400
500
600
700
800
0
5
10
15
20
25
30
35
Time (h)
Flow direction
ū_r away from center (µm) [with flow]
0.6
0
-0.6
ū_r towards center (µm) [against flow]
C
Intermitent flow
Static
Cell migration speed (µm/h)
ns
**
ns
2
1
0
D
Correlation length (µm)
ns
*
*
200
150
100
50
0
Static (0-5 h)
Flow (5-25 h)
Static (25-35 h)

Fig. 3: Flow exposure reduces µEC migration speed with gradual recovery after flow cessation.

A Representative phase contrast images, cell migration speed (µm/h), and cell displacement vectors (scaled 15x) for HMEC-1 in monolayer at different time points. Cells were imaged without flow for ~5 h, followed by 20 h during flow (between dashed black lines) and an additional 10 h under static conditions after flow cessation. Jet center positioned at the center of the field of view imaged, but only a quarter of the field of view is shown. White or black contours mark concentric regions spaced 185 µm apart from the jet orifice. **B** Kymograph of mean radial cell displacements u_r (µm) over radial distance r (µm), for the same representative HMEC-1 recording as shown in panel a. The 20 h flow period is marked by dashed black lines. **C** Bar plot showing the mean cell migration speed (y-axis, µm/h) of HMEC-1 maintained under static conditions throughout the experiment (gray) or exposed intermittently to flow (red). Averaging was performed over three time windows: 0–5 h after the start of recording, during which both groups were under static conditions; 5–25 h, during which the intermittent-flow group was exposed to flow; and 25–35 h, during which both groups were again under static conditions. Mean±SD, N=6 independent recordings. Superimposed circles show average values for independent recordings. WRST, $p>0.05$: non-significant, ns; $p<0.05$: *; $p<0.01$: **. **D** Same as panel C, but showing mean correlation length (y-axis, µm) of cell motion.

Figure 4

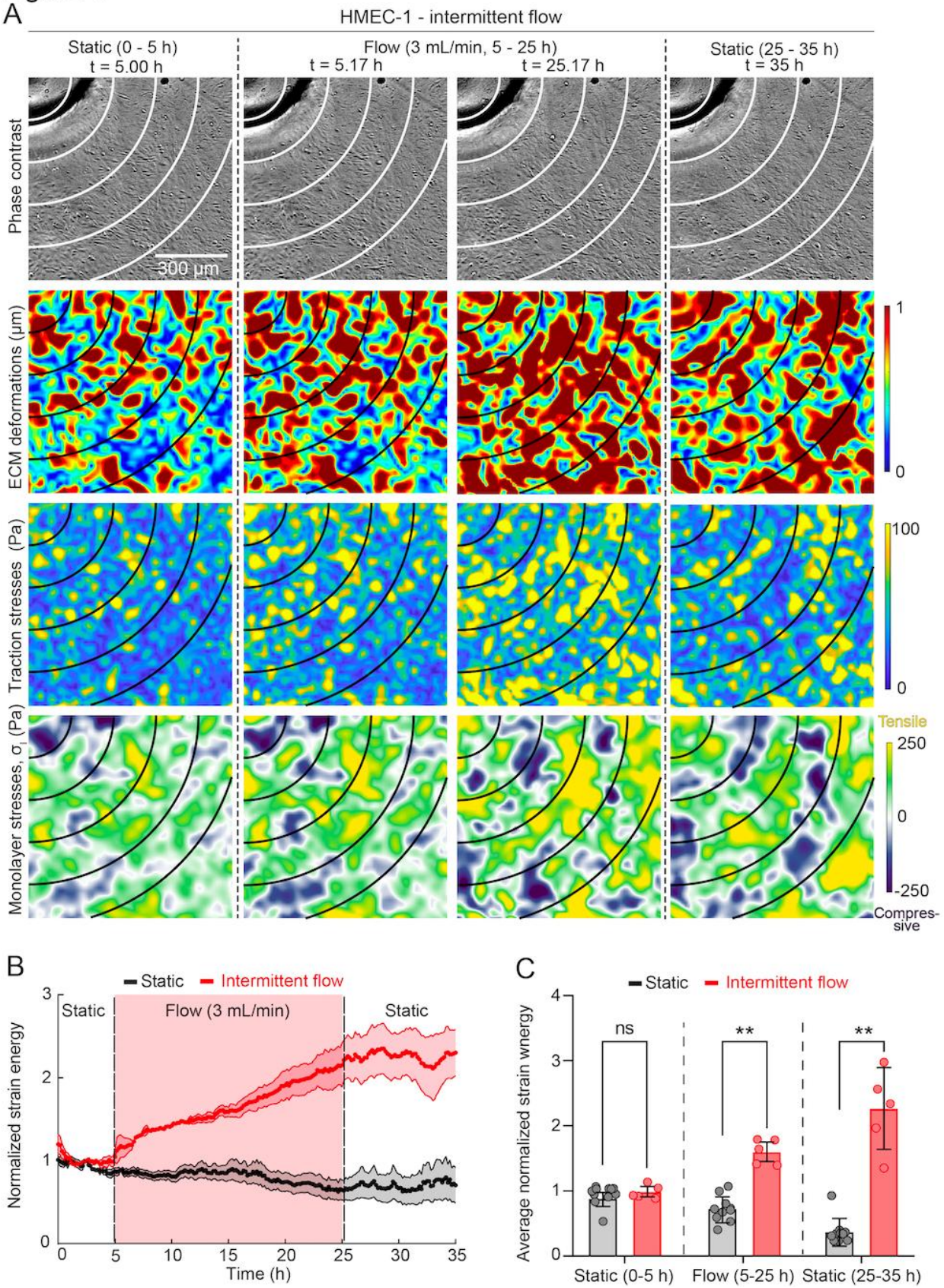

A
HMEC-1 - intermittent flow
Static (0 - 5 h)
t = 5.00 h
Flow (3 mL/min, 5 - 25 h)
t = 5.17 h
t = 25.17 h
Static (25 - 35 h)
t = 35 h
Phase contrast
300 µm
ECM deformations (µm)
1
0
Traction stresses (Pa)
100
0
Monolayer stresses, σ1 (Pa)
Tensile
250
0
-250
Compres-sive
B
Static
Intermittent flow
Static
Flow (3 mL/min)
Static
Normalized strain energy
Time (h)
C
Static
Intermittent flow
ns
**
**
Average normalized strain wnergy
Static (0-5 h)
Flow (5-25 h)
Static (25-35 h)

Fig. 4: Flow induces a quasi-linear increase in cellular traction and monolayer stresses.
A Representative images of HMEC-1 in monolayer at various stages: before flow (1st column), immediately after flow initiation (2nd), 20 h into flow (3rd), and 10 h post-flow cessation (4th). Rows show phase contrast (1st), ECM deformations (2nd, µm), cellular traction stresses (3rd, Pa), and monolayer tensile stresses, σ_1 (4th, Pa). Cells on a 3 kPa matrix were exposed to flow using the impinging flow device. Jet center positioned at the center of the field of view imaged, but only a quarter of the field of view is shown. White or black contours mark concentric regions spaced 185 µm apart from the jet orifice. **B** Normalized strain energy (i.e., mechanical work imparted by HMEC-1) over time. Red line (intermittent flow-exposed) refers to cells that were initially under static conditions (0–5 h), exposed to flow (5–25 h, red shading), and then under static conditions again (25–35 h). Black line refers to control cells never exposed to flow. Mean±SEM, n 7±2 recordings analyzed originating from N=3 independent experiments. Strain energy is normalized to its initial value at the first time point of the recording. **C** Bar plots of time-averaged normalized strain energy as in panel B, binned by experimental recording phase: pre-flow (0–5 h), flow (5–25 h), and post-flow (25–35 h). Red bars: intermittent flow-exposed cells; black bars: static controls. Mean±SD. WRST, $p>0.05$: ns; $p<0.05$: *; $p<0.01$: **.

Figure 5

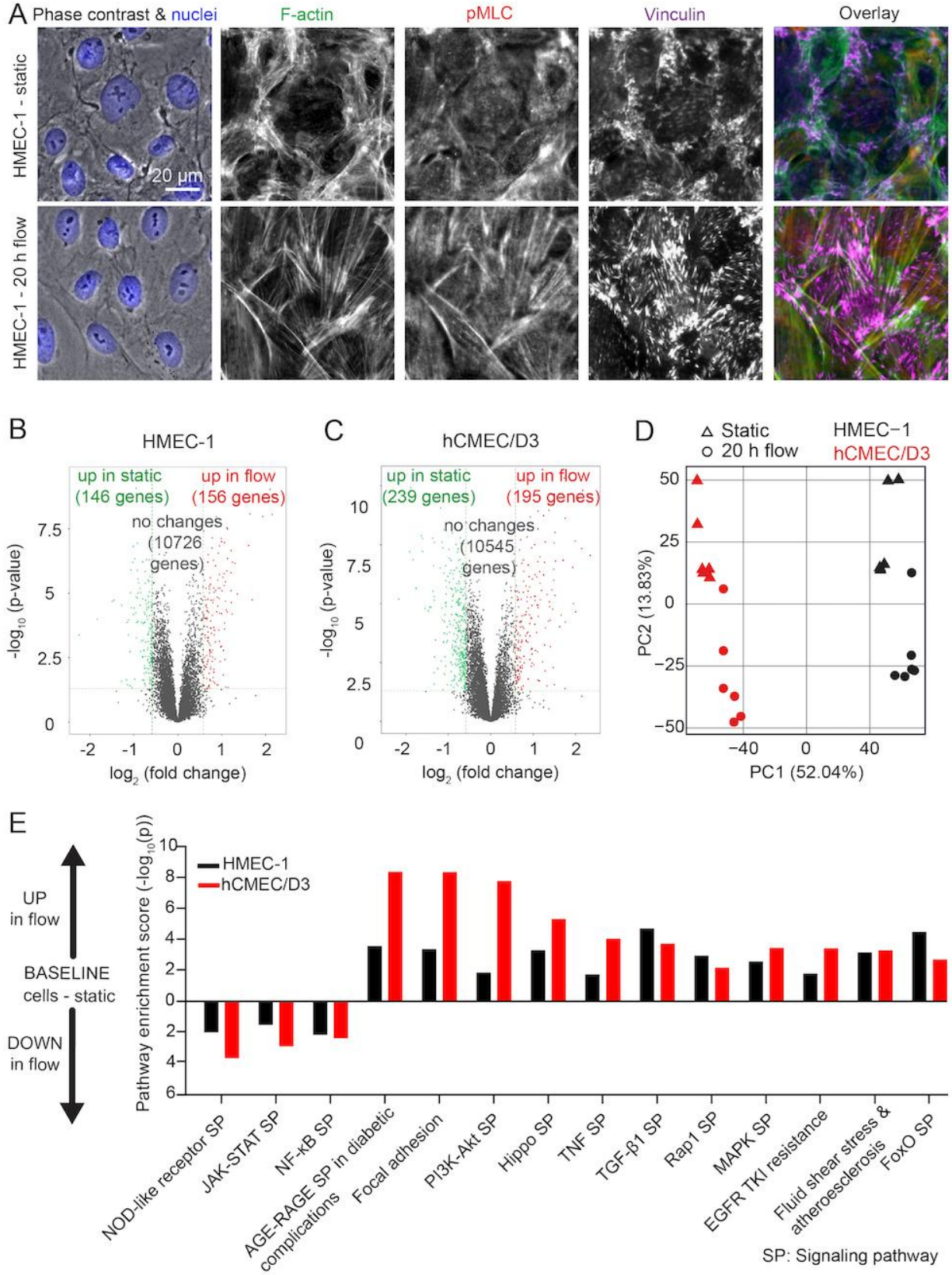

A
Phase contrast & nuclei
F-actin
pMLC
Vinculin
Overlay
HMEC-1 - static
HMEC-1 - 20 h flow
20 µm
B
HMEC-1
up in static (146 genes)
up in flow (156 genes)
no changes (10726 genes)
-log10 (p-value)
log2 (fold change)
C
hCMEC/D3
up in static (239 genes)
up in flow (195 genes)
no changes (10545 genes)
-log10 (p-value)
log2 (fold change)
D
Static
20 h flow
HMEC−1
hCMEC/D3
PC2 (13.83%)
PC1 (52.04%)
E
UP in flow
BASELINE cells - static
DOWN in flow
Pathway enrichment score (-log10(p))
HMEC-1
hCMEC/D3
NOD-like receptor SP
JAK-STAT SP
NF-κB SP
AGE-RAGE SP in diabetic complications
Focal adhesion
PI3K-Akt SP
Hippo SP
TNF SP
TGF-β1 SP
Rap1 SP
MAPK SP
EGFR TKI resistance
Fluid shear stress & atheroesclerosis
FoxO SP
SP: Signaling pathway

Fig. 5: SSG induces alterations in the cytoskeleton and gene expression in µEC.

A Immunofluorescence images of HMEC-1 cells following static culture (1st row) or 20 h flow exposure (2nd). Columns display: phase contrast (grayscale) overlaid with cell nuclei (blue); F-actin (green in overlay); phosphorylated myosin-light chain (pMLC, red in overlay), vinculin (magenta in overlay); and a composite overlay of these signals. **B-C** Volcano plots of DEGs for HMEC-1 (B) and hCMEC/D3 (C) exposed for 20 h to shear flow versus not (static condition). The $-\log_{10}$ p-values (y-axis) are plotted against the average $\log_2$-fold changes in expression (x-axis). For each cell type, upregulated genes in flow-exposed cells are shown in red, downregulated in green, and non-DEGs in gray. N=6 biological replicates per condition. **D** PCA on top genes that have ANOVA p value ≤ 0.05 on FPKM abundance estimations. PC1 versus PC2. HMEC-1: black; hCMEC/D3: red; cells under static conditions: triangle; and cells exposed to flow for 20 h: circle. **E** HMEC-1 (black) and hCMEC/D3 (red) cells exposed to shear flow for 20 h were compared with static (no-flow) controls based on their pathway enrichment score ($-\log_{10}$p). Shown are pathways that are commonly up- or down-regulated in both cell types with respect to cells under static conditions and have a mean enrichment score > 1.5.

Figure 6

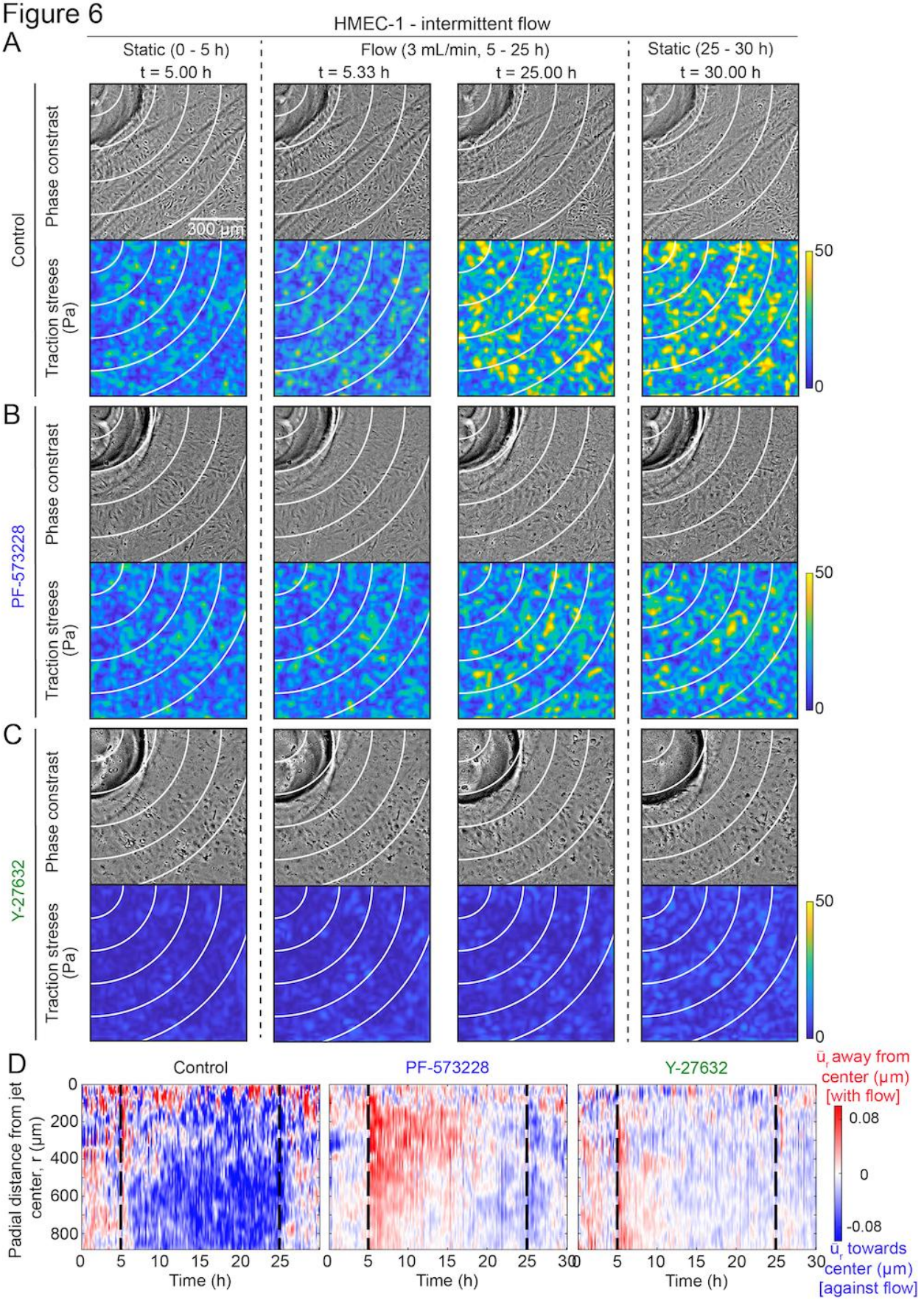

A
HMEC-1 - intermittent flow
Static (0 - 5 h)
Flow (3 mL/min, 5 - 25 h)
Static (25 - 30 h)
t = 5.00 h
t = 5.33 h
t = 25.00 h
t = 30.00 h
Control
Phase constrast
Traction streses (Pa)
300 µm
50
0
B
PF-573228
C
Y-27632
D
Control
PF-573228
Y-27632
Padial distance from jet center, r (µm)
Time (h)
ū_r away from center (µm) [with flow]
0.08
0
-0.08
ū_r towards center (µm) [against flow]

Fig. 6: The FAK and ROCK signaling pathways regulate μEC rheotaxis and dynamics.
A Representative images of HMEC-1 in monolayer at various stages: before flow exposure (1st column), immediately after flow initiation (2nd), 20 h into flow (3rd), and 5 h post-flow cessation (4th). Rows show phase contrast (1st) and cellular traction stresses (2nd, Pa). Cells on a 3 kPa matrix were exposed to flow using the impinging flow device. Jet center positioned at the center of the field of view imaged, but only a quarter of the field of view is shown. White or black contours mark concentric regions spaced 185 μm apart from the jet orifice. **B-C** Same as panel A but for cells treated with 5 μM PF537228 (B) or 10 μM Y-27632 (C). **D** Kymograph of mean radial cell displacements u_r (μm) over radial distance r (μm), for HMEC-1 in monolayer for the representative recordings shown in panels A-C. In the left kymograph, cells were treated with vehicle control, middle kymograph with PF537228 and right kymograph with Y-27632 (right). The flow exposure period is indicated between black dashed lines.

Figure 7

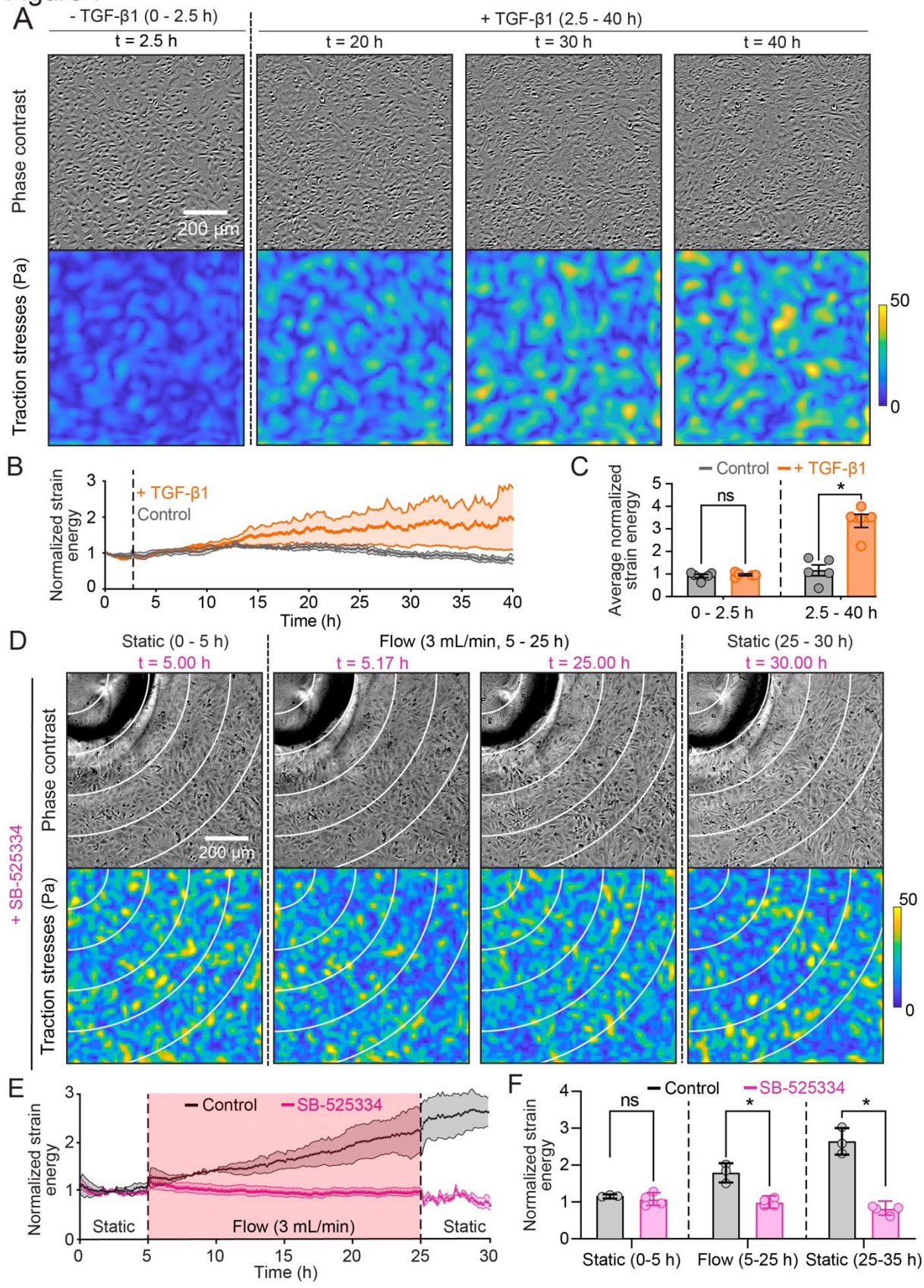

A
- TGF-β1 (0 - 2.5 h)
+ TGF-β1 (2.5 - 40 h)
t = 2.5 h
t = 20 h
t = 30 h
t = 40 h
Phase contrast
200 μm
Traction stresses (Pa)
50
0
B
Normalized strain energy
+ TGF-β1
Control
Time (h)
C
Control
+ TGF-β1
Average normalized strain energy
ns
*
0 - 2.5 h
2.5 - 40 h
D
Static (0 - 5 h)
Flow (3 mL/min, 5 - 25 h)
Static (25 - 30 h)
t = 5.00 h
t = 5.17 h
t = 25.00 h
t = 30.00 h
+ SB-525334
Phase contrast
200 μm
Traction stresses (Pa)
50
0
E
Control
SB-525334
Normalized strain energy
Static
Flow (3 mL/min)
Static
Time (h)
F
Control
SB-525334
ns
*
*
Normalized strain energy
Static (0-5 h)
Flow (5-25 h)
Static (25-35 h)

Fig. 7: The increase in EC traction stresses upon flow exposure depends on TGF-β1.
A Representative images of HMEC-1 in monolayer under static condition in the presence of 10 ng/mL TGF-β1. Note that TGF-β1 was added 2.5 h post-initiation of the microscopy recording. Columns show different time points. Rows show corresponding phase contrast image (top) and cellular traction stresses (bottom, Pa). **B** Normalized strain energy of HMEC-1 in monolayer under static conditions treated with vehicle control (gray) or 10 ng/mL TGF-β1 (orange) over time (h). Strain energy is normalized to the first value at the beginning of each recording. Mean±SEM, N=4 independent experiments. **C** Bar plot of average normalized strain energy of data shown in panel B binned by time periods of 0-2.5 h (no TGF- β1) and 2.5-40 h (addition of TGF- β1) for HMEC-1 treated with TGF-β1 (orange) or not (gray). Mean±SD. WRST, $p>0.05$: ns; $p<0.05$: *. **D** Representative images of HMEC-1 in monolayer treated with 10 μM SB-525334 at different instant of time, namely: before flow (1st column), immediately after flow initiation (2nd), 20 h into flow (3rd), and 5 h post-flow cessation (4th). Rows show phase contrast (1st) and cellular traction stresses (2nd, Pa). Cells on a 3 kPa matrix were exposed to flow using the impinging flow device. Jet center positioned at the center of the field of view imaged, but only a quarter of the field of view is shown. White or black contours mark concentric regions spaced 185 μm apart from the jet orifice. **E** Normalized strain energy of HMEC-1 in monolayer treated with vehicle control (black) or 10 μM SB-525334 (magenta) over time (h). Strain energy is normalized with respect to the first value at the beginning of each recording. Mean±SEM, N=3-4 independent TFM recordings. Time of flow exposure is shown in red shade. **F** Bar plot of average normalized strain energy of data shown in panel E binned by time periods of 0-5 h (static), 5-25 h (flow) and 25-30 h (static) for exposed to SB-525334 (magenta) or vehicle control (black). Mean±SD. WRST, $p>0.05$: ns; $p<0.05$: *.

REFERENCES

1. Davies, P.F. Hemodynamic shear stress and the endothelium in cardiovascular pathophysiology. *Nat Clin Pract Cardiovasc Med* **6**, 16-26 (2009).
2. Chiu, J.J. & Chien, S. Effects of Disturbed Flow on Vascular Endothelium: Pathophysiological Basis and Clinical Perspectives. *Physiol Rev* **91**(2011).
3. Zhou, J., Li, Y.S. & Chien, S. Shear stress-initiated signaling and its regulation of endothelial function. *Arterioscler Thromb Vasc Biol* **34**, 2191-2198 (2014).
4. Dessalles, C.A., Leclech, C., Castagnino, A. & Barakat, A.I. Integration of substrate- and flow-derived stresses in endothelial cell mechanobiology. *Commun. Biol.* **4**, 764 (2021).
5. Maurya, M.R.*, et al.* Longitudinal shear stress response in human endothelial cells to atheroprone and atheroprotective conditions. *Proc Natl Acad Sci U S A* **118**(2021).
6. Papaioannou, T.G. & Stefanadis, C. Vascular wall shear stress: basic principles and methods. *Hellenic J Cardiol* **46**, 9-15 (2005).
7. Dolan, J.M., Kolega, J. & Meng, H. High wall shear stress and spatial gradients in vascular pathology: a review. *Ann Biomed Eng* **41**, 1411-1427 (2013).
8. Grandchamp, X., Coupier, G., Srivastav, A., Minetti, C. & Podgorski, T. Lift and down-gradient shear-induced diffusion in red blood cell suspensions. *Phys. Rev. Lett.* **110**, 108101 (2013).
9. Tarbell, J.M. Shear stress and the endothelial transport barrier. *Cardiovasc. Res.* **87**, 320-330 (2010).
10. Ostrowski, M.A.*, et al.* Multiplexed Fluid Flow Device to Study Cellular Response to Tunable Shear Stress Gradients. *Ann Biomed Eng* **44**, 2261-2272 (2016).
11. Surya, V.N., Michalaki, E., Fuller, G.G. & Dunn, A.R. Lymphatic endothelial cell calcium pulses are sensitive to spatial gradients in wall shear stress. *Mol. Biol. Cell* **30**, 923-931 (2019).
12. Ostrowski, Maggie A.*, et al.* Microvascular Endothelial Cells Migrate Upstream and Align Against the Shear Stress Field Created by Impinging Flow. *Biophys. J.* **106**, 366-374 (2014).
13. Lee, H.-W., Shin, J.H. & Simons, M. Flow goes forward and cells step backward: endothelial migration. *Exp. Mol. Med.* **54**, 711-719 (2022).
14. Xiao, R., Liu, J. & Shawn Xu, X.Z. Mechanosensitive GPCRs and ion channels in shear stress sensing. *Curr. Opin. Cell Biol.* **84**, 102216 (2023).
15. Bartosch, A.M.W.*, et al.* Heparan sulfate proteoglycan glypican-1 and PECAM-1 cooperate in shear-induced endothelial nitric oxide production. *Sci. Rep.* **11**, 11386 (2021).
16. X, S.*, et al.* Controversy in mechanotransduction – the role of endothelial cell–cell junctions in fluid shear stress sensing. *J. Cell Sci.* **137**, jcs262348 (2024).
17. Michalaki, E., Surya, V.N., Fuller, G.G. & Dunn, A.R. Perpendicular alignment of lymphatic endothelial cells in response to spatial gradients in wall shear stress. *Commun Biol* **3**, 57 (2020).
18. Michalaki, E., Surya, V.N., Rodríguez-Hakim, M., Fuller, G.G. & Dunn, A.R. Response of lymphatic endothelial cells to combined spatial and temporal variations in fluid flow. *Faseb j* **37**, e23240 (2023).
19. Hur, S.S.*, et al.* Roles of cell confluency and fluid shear in 3-dimensional intracellular forces in endothelial cells. *Proc Natl Acad Sci U S A* **109**, 11110-11115 (2012).
20. Ting, L.H.*, et al.* Flow mechanotransduction regulates traction forces, intercellular forces, and adherens junctions. *Am J Physiol Heart Circ Physiol* **302**, H2220-2229 (2012).
21. Barbacena, P.*, et al.* Competition for endothelial cell polarity drives vascular morphogenesis. *Dev. Cell* **57**, 2321-2333.e2329 (2022).

22. Steward, R., Tambe, D., Hardin, C.C., Krishnan, R. & Fredberg, J.J. Fluid shear, intercellular stress, and endothelial cell alignment. *Am. J. Physiol. Cell Physiol.* **308**, C657-C664 (2015).
23. Cheng, C.K., Wang, N., Wang, L. & Huang, Y. Biophysical and Biochemical Roles of Shear Stress on Endothelium: A Revisit and New Insights. *Circ. Res.* **136**, 752-772 (2025).
24. Baeyens, N.*, et al.* Vascular remodeling is governed by a VEGFR3-dependent fluid shear stress set point. *Elife* **4**(2015).
25. Mehta, A.*, et al.* Bio-Mimicking Brain Vasculature to Investigate the Role of Heterogeneous Shear Stress in Regulating Barrier Integrity. *Adv Biol (Weinh)* **6**, e2200152 (2022).
26. Balogh, P. & Bagchi, P. Three-dimensional distribution of wall shear stress and its gradient in red cell-resolved computational modeling of blood flow in in vivo-like microvascular networks. *Physiol. Rep.* **7**, e14067 (2019).
27. Angelini, T.E., Hannezo, E., Trepat, X., Fredberg, J.J. & Weitz, D.A. Cell migration driven by cooperative substrate deformation patterns. *Phys Rev Lett* **104**, 168104 (2010).
28. Bastounis, E.E., Yeh, Y.T. & Theriot, J.A. Subendothelial stiffness alters endothelial cell traction force generation while exerting a minimal effect on the transcriptome. *Sci Rep* **9**, 18209 (2019).
29. Hardin, C.*, et al.* Glassy dynamics, cell mechanics, and endothelial permeability. *J. Phys. Chem. B* **117**, 12850-12856 (2013).
30. Buscemi, L.*, et al.* The Single-Molecule Mechanics of the Latent TGF-β1 Complex. *Curr. Biol.* **21**, 2046-2054 (2011).
31. Daubon, T.*, et al.* Deciphering the complex role of thrombospondin-1 in glioblastoma development. *Nat. Commun.* **10**, 1146 (2019).
32. Ahamed, J., Janczak, C.A., Wittkowski, K.M. & Coller, B.S. In vitro and in vivo evidence that thrombospondin-1 (TSP-1) contributes to stirring- and shear-dependent activation of platelet-derived TGF-beta1. *PLoS One* **4**, e6608 (2009).
33. Ramachandran, A.*, et al.* JunB mediates basal- and TGFβ1-induced smooth muscle cell contractility. *PLoS One* **8**, e53430 (2013).
34. Luettich, K. & Schmidt, C. TGFβ1 activates c-Jun and Erk1 via αVβ6 integrin. *Mol. Cancer* **2**, 33 (2003).
35. Pierce, G.F.*, et al.* Platelet-derived growth factor and transforming growth factor-beta enhance tissue repair activities by unique mechanisms. *J Cell Biol* **109**, 429-440 (1989).
36. Sumpio, B.E.*, et al.* Regulation of PDGF-B in Endothelial Cells Exposed to Cyclic Strain. *Arterioscler. Thromb. Vasc. Biol.* **18**, 349-355 (1998).
37. Mondy, J.S.*, et al.* Platelet-derived growth factor ligand and receptor expression in response to altered blood flow in vivo. *Circ Res* **81**, 320-327 (1997).
38. Yan, X., Liu, Z. & Chen, Y. Regulation of TGF-beta signaling by Smad7. *Acta Biochim Biophys Sin (Shanghai)* **41**, 263-272 (2009).
39. Yashiro, R.*, et al.* Transforming growth factor-beta stimulates interleukin-11 production by human periodontal ligament and gingival fibroblasts. *J Clin Periodontol* **33**, 165-171 (2006).
40. Lerrer, S.*, et al.* Co-Inflammatory Roles of TGFβ1 in the Presence of TNFα Drive a Pro-inflammatory Fate in Mesenchymal Stem Cells. *Front Immunol* **8**, 479 (2017).
41. Li, G.*, et al.* Caveolin-1 and Its Functional Peptide CSP7 Affect Silica-Induced Pulmonary Fibrosis by Regulating Fibroblast Glutaminolysis. *Toxicol Sci* **190**, 41-53 (2022).
42. Ungefroren, H., Witte, D. & Lehnert, H. The role of small GTPases of the Rho/Rac family in TGF-β-induced EMT and cell motility in cancer. *Dev Dyn* **247**, 451-461 (2018).

43. Shiu, Y.T.*, et al.* Rho mediates the shear-enhancement of endothelial cell migration and traction force generation. *Biophys J* **86**, 2558-2565 (2004).
44. Brandt, M., Gerke, V. & Betz, T. Human endothelial cells display a rapid tensional stress increase in response to tumor necrosis factor-α. *PLoS One* **17**, e0270197 (2022).
45. Conway, Daniel E.*, et al.* Fluid Shear Stress on Endothelial Cells Modulates Mechanical Tension across VE-Cadherin and PECAM-1. *Curr. Biol.* **23**, 1024-1030 (2013).
46. Santana Nunez, D.*, et al.* Piezo1 induces endothelial responses to shear stress via soluble adenylyl Cyclase-IP3R2 circuit. *iScience* **26**, 106661 (2023).
47. Chuntharpursat-Bon, E.*, et al.* PIEZO1 and PECAM1 interact at cell-cell junctions and partner in endothelial force sensing. *Commun. Biol.* **6**, 358 (2023).
48. Givens, C. & Tzima, E. Endothelial Mechanosignaling: Does One Sensor Fit All? *Antioxid Redox Signal* **25**, 373-388 (2016).
49. Charbonier, F.W., Zamani, M. & Huang, N.F. Endothelial Cell Mechanotransduction in the Dynamic Vascular Environment. *Adv Biosyst* **3**, e1800252 (2019).
50. Carey, S.P.*, et al.* Local extracellular matrix alignment directs cellular protrusion dynamics and migration through Rac1 and FAK. *Integr. Biol.* **8**, 821-835 (2016).
51. Polacheck, W.J., German, A.E., Mammoto, A., Ingber, D.E. & Kamm, R.D. Mechanotransduction of fluid stresses governs 3D cell migration. *Proc Natl Acad Sci U S A* **111**, 2447-2452 (2014).
52. Li, S.*, et al.* The role of the dynamics of focal adhesion kinase in the mechanotaxis of endothelial cells. *Proc Natl Acad Sci U S A* **99**, 3546-3551 (2002).
53. Fernández-Yagüe, M.A.*, et al.* Mechanochemical waves in focal adhesions during cell migration. *Sci Adv* **11**, eadw6425 (2025).
54. Jerrell, R.J., Leih, M.J. & Parekh, A. The altered mechanical phenotype of fetal fibroblasts hinders myofibroblast differentiation. *Wound Repair Regen* **27**, 29-38 (2019).
55. Kim, K.K., Sheppard, D. & Chapman, H.A. TGF-β1 Signaling and Tissue Fibrosis. *Cold Spring Harb Perspect Biol* **10**(2018).
56. Keski-Oja, J., Koli, K. & von Melchner, H. TGF-β activation by traction? *Trends Cell Biol.* **14**, 657-659 (2004).
57. Hinz, B. The extracellular matrix and transforming growth factor-β1: Tale of a strained relationship. *Matrix Biol* **47**, 54-65 (2015).
58. Wang, H., Li, M., Lin, P.H., Yao, Q. & Chen, C. Fluid Shear Stress Regulates the Expression of TGF-β1 and Its Signaling Molecules in Mouse Embryo Mesenchymal Progenitor Cells. *J. Surg. Res.* **150**, 266-270 (2008).
59. Birukova, A.A., Rios, A. & Birukov, K.G. Long-term cyclic stretch controls pulmonary endothelial permeability at translational and post-translational levels. *Exp Cell Res* **314**, 3466-3477 (2008).
60. Birukov, K.G.*, et al.* Magnitude-dependent regulation of pulmonary endothelial cell barrier function by cyclic stretch. *Am J Physiol Lung Cell Mol Physiol* **285**, L785-797 (2003).
61. Luo, J.*, et al.* Tissue-Engineered Vascular Grafts with Advanced Mechanical Strength from Human iPSCs. *Cell Stem Cell* **26**, 251-261.e258 (2020).
62. Chandurkar, M.K.*, et al.* Transient low shear-stress preconditioning influences long-term endothelial traction and alignment under high shear flow. *Am J Physiol Heart Circ Physiol* **326**, H1180-h1192 (2024).
63. Yates, A.K.*, et al.* Substrate stiffness and shear stress collectively regulate the inflammatory phenotype in cultured human brain microvascular endothelial cells. *Fluids Barriers CNS* **22**, 73 (2025).
64. Clark, P.R., Manes, T.D., Pober, J.S. & Kluger, M.S. Increased ICAM-1 expression causes endothelial cell leakiness, cytoskeletal reorganization and junctional alterations. *J Invest Dermatol* **127**, 762-774 (2007).

65. Bai, B.*, et al.* NLRP3 inflammasome in endothelial dysfunction. *Cell Death Dis* **11**, 776 (2020).
66. Wang, L.*, et al.* Suppressing STAT3 activity protects the endothelial barrier from VEGF-mediated vascular permeability. *Dis Model Mech* **14**, dmm049029 (2021).
67. Schneider, C.A., Rasband, W.S. & Eliceiri, K.W. NIH Image to ImageJ: 25 years of image analysis. *Nat. Methods* **9**, 671-675 (2012).
68. Gui, L. & Wereley, S.T. A correlation-based continuous window-shift technique to reduce the peak-locking effect in digital PIV image evaluation. *Exp. Fluids* **32**, 506-517 (2002).
69. Bastounis, E.E., Ortega, F.E., Serrano, R. & Theriot, J.A. A Multi-well Format Polyacrylamide-based Assay for Studying the Effect of Extracellular Matrix Stiffness on the Bacterial Infection of Adherent Cells. *J Vis Exp* (2018).
70. del Álamo, J.C.*, et al.* Spatio-temporal analysis of eukaryotic cell motility by improved force cytometry. *Proc. Nat. Acad. Sci.* **104**, 13343-13348 (2007).
71. Lamason, R.L.*, et al.* Rickettsia Sca4 Reduces Vinculin-Mediated Intercellular Tension to Promote Spread. *Cell* **167**, 670-683.e610 (2016).
72. Bastounis, E.*, et al.* Both contractile axial and lateral traction force dynamics drive amoeboid cell motility. *J. Cell Biol.* **204**, 1045-1061 (2014).
73. Yuste, R.A.*, et al.* Borrelia burgdorferi modulates the physical forces and immunity signaling in endothelial cells. *iScience* **25**, 104793 (2022).
74. Muenkel, M., Aparicio-Yuste, R., Tal, M.C., Kraiczy, P. & Bastounis, E.E. Spatiotemporal characterization of endothelial cell motility and physical forces during exposure to Borrelia burgdorferi. *STAR Protocols* **3**, 101832 (2022).
75. Selinummi, J., Seppala, J., Yli-Harja, O. & Puhakka, J.A. Software for quantification of labeled bacteria from digital microscope images by automated image analysis. *Biotechniques* **39**, 859-863 (2005).

Supplementary Files

This is a list of supplementary files associated with this preprint. Click to download.

- SupplementalmaterialSanchezetal20260420.pdf
- SupplementaryTable1.xlsx
- SupplementaryVideo4.mp4
- SupplementaryVideo1.mp4
- SupplementaryVideo2.mp4
- SupplementaryVideo5.mp4
- SupplementaryVideo3.mp4